PMR 5251

Assessment of Mechanical Behavior of Materials using Machine Learning Approach

Profa.Dra. Izabel Fernanda Machado and

Profa. Dra. Larissa Driemeier

Profa. Izabel Machado - machadoi@usp.br
Profa. Larissa Driemeier - driemeie@usp.br

Damage and Failure analysis – microstructure heterogeneities stress intensifiers, nucleation and growth of cracks

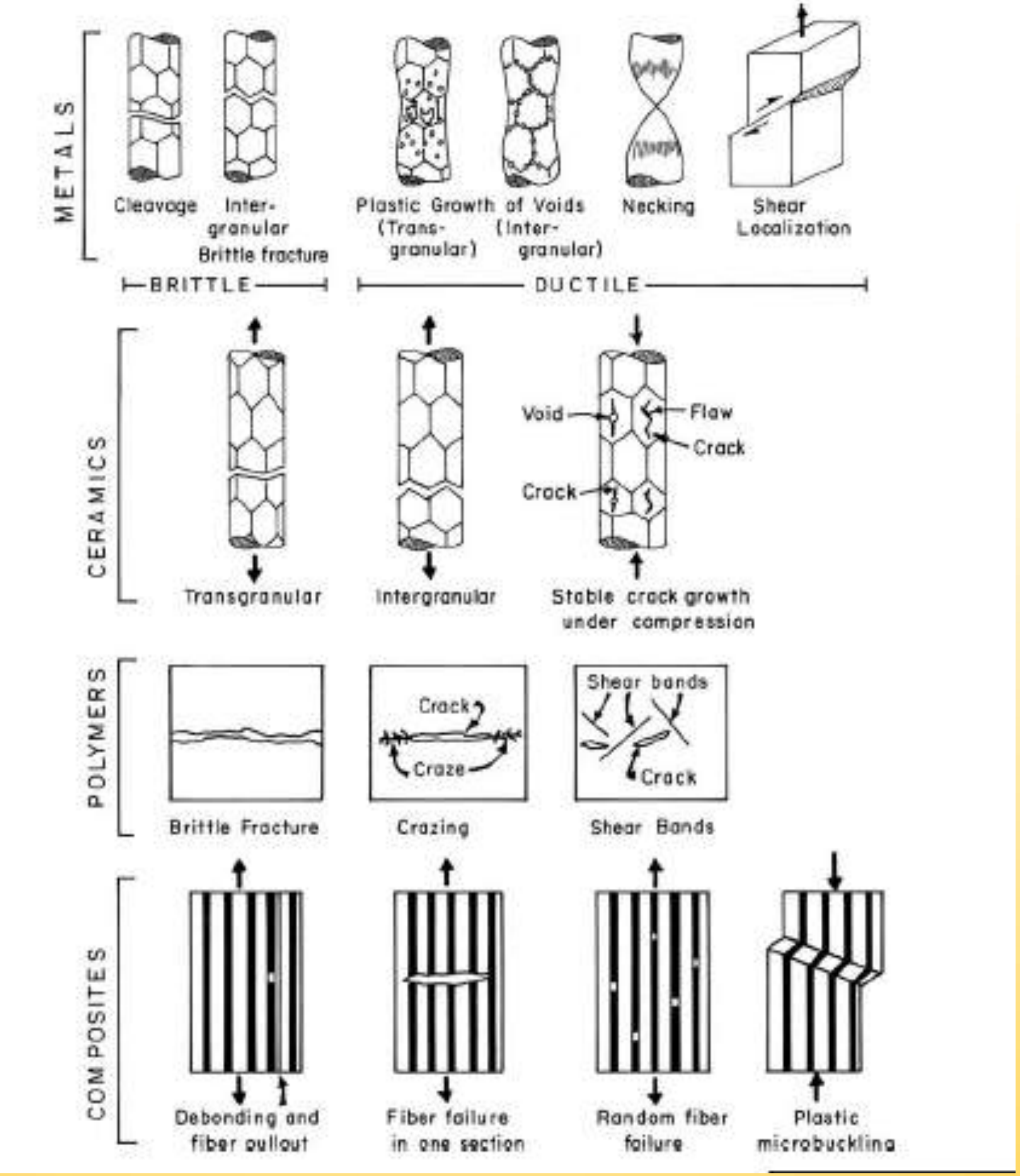

Damage and Failure analysis – microstructure heterogeneities stress intensifiers, nucleation and growth of cracks

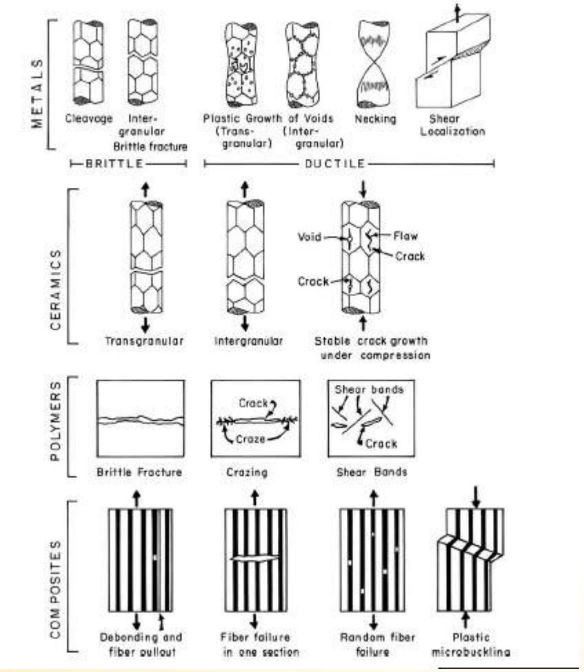

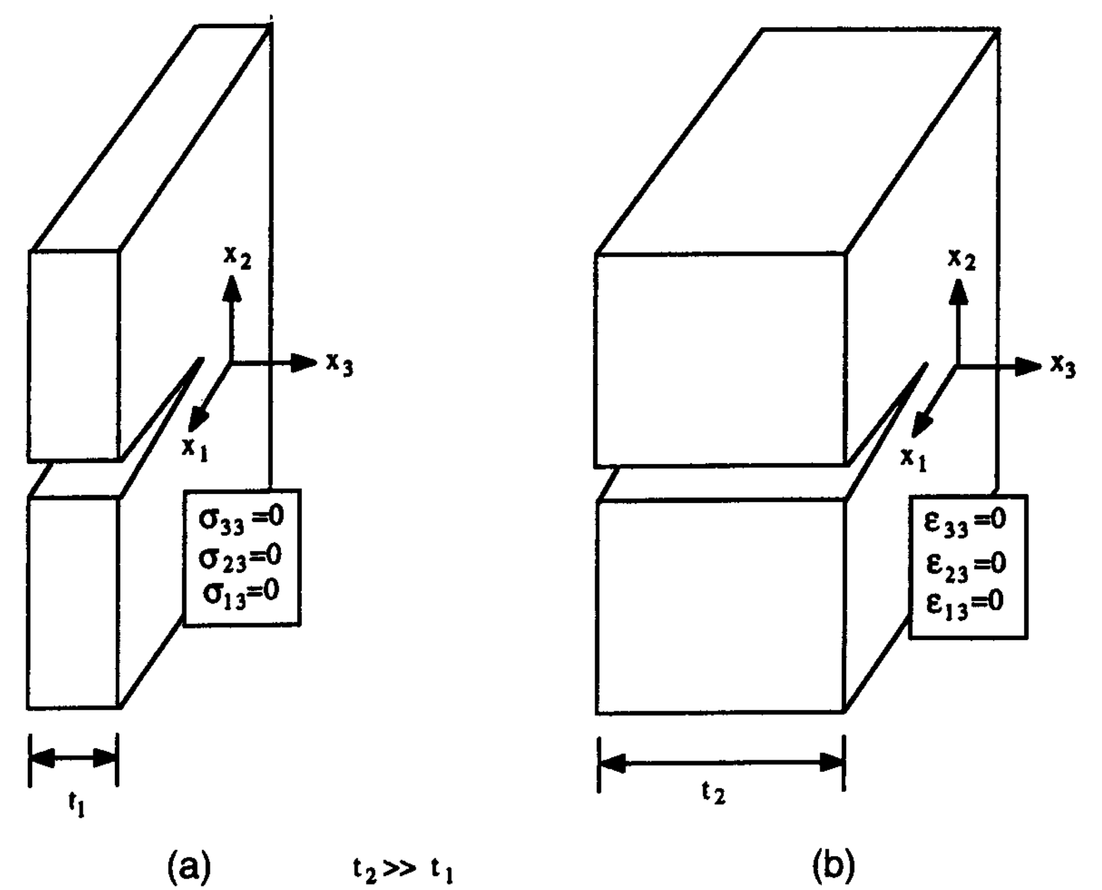

Figure 7.7 Crack in (a) thin (t_1) and (b) thick (t_2) plates. Note the plane-stress state in (a) and the plane-strain state in (b).

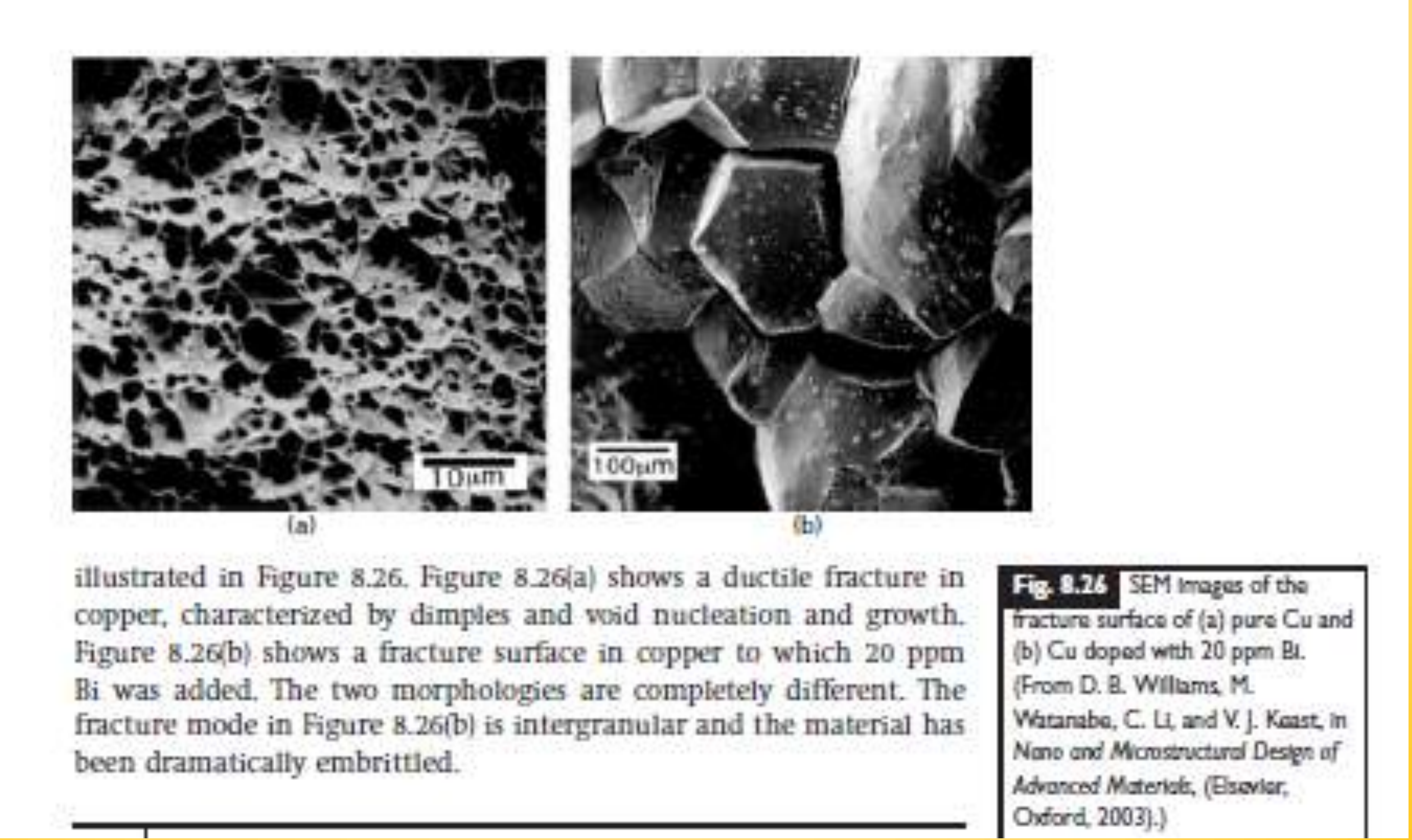

illustrated in Figure 8.26. Figure 8.26(a) shows a ductile fracture in copper, characterized by dimples and void nucleation and growth. Figure 8.26(b) shows a fracture surface in copper to which 20 ppm Bi was added. The two morphologies are completely different. The fracture mode in Figure 8.26(b) is intergranular and the material has been dramatically embrittled.

Fig. 8.26 SEM images of the fracture surface of (a) pure Cu and (b) Cu doped with 20 ppm Bi. (From D. B. Williams, M. Watanabe, C. Li, and V. J. Keast, in *Nano and Microstructural Design of Advanced Materials*, (Elsevier, Oxford, 2003).)

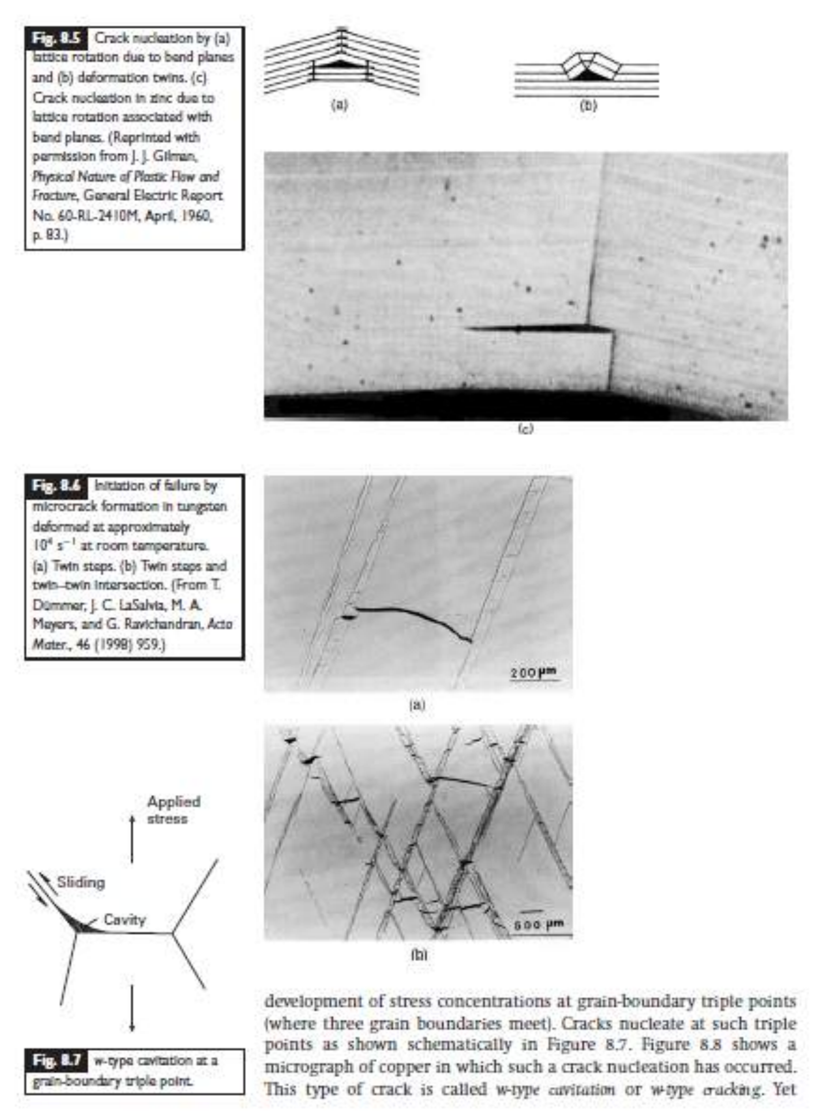

Fig. 8.5 Crack nucleation by (a) lattice rotation due to bend planes and (b) deformation twins. (c) Crack nucleation in zinc due to lattice rotation associated with bend planes. (Reprinted with permission from J. J. Gilman, *Physical Nature of Plastic Flow and Fracture*, General Electric Report No. 60-RL-2410M, April, 1960, p. 83.)

Fig. 8.6 Initiation of failure by microcrack formation in tungsten deformed at approximately 10^4 s^{-1} at room temperature. (a) Twin steps. (b) Twin steps and twin–twin intersection. (From T. Dümmer, J. C. LaSalvia, M. A. Meyers, and G. Ravichandran, *Acta Mater.*, 46 (1998) 959.)

Fig. 8.7 w-type cavitation at a grain-boundary triple point.

development of stress concentrations at grain-boundary triple points (where three grain boundaries meet). Cracks nucleate at such triple points as shown schematically in Figure 8.7. Figure 8.8 shows a micrograph of copper in which such a crack nucleation has occurred. This type of crack is called *w-type cavitation* or *w-type cracking*. Yet

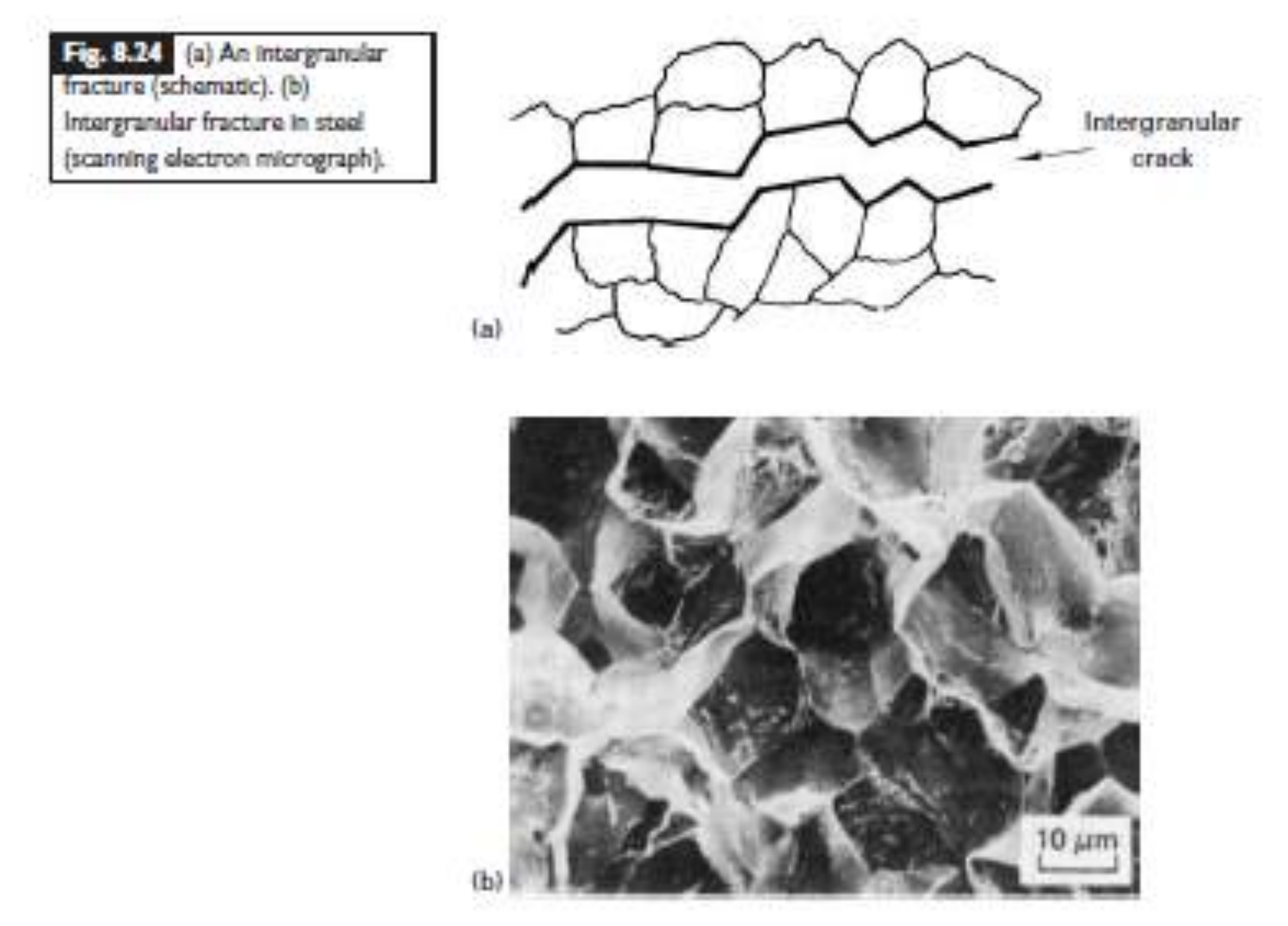

Fig. 8.24 (a) An intergranular fracture (schematic). (b) Intergranular fracture in steel (scanning electron micrograph).

Hot cracking behavior and mechanism of a third-generation Ni-based single- crystal superalloy during directed energy deposition

Damage and Failure analysis – microstructure heterogeneities stress intensifiers, nucleation and growth of cracks

N. Lu, et al. *Additive Manufacturing 34 (2020) 101228*

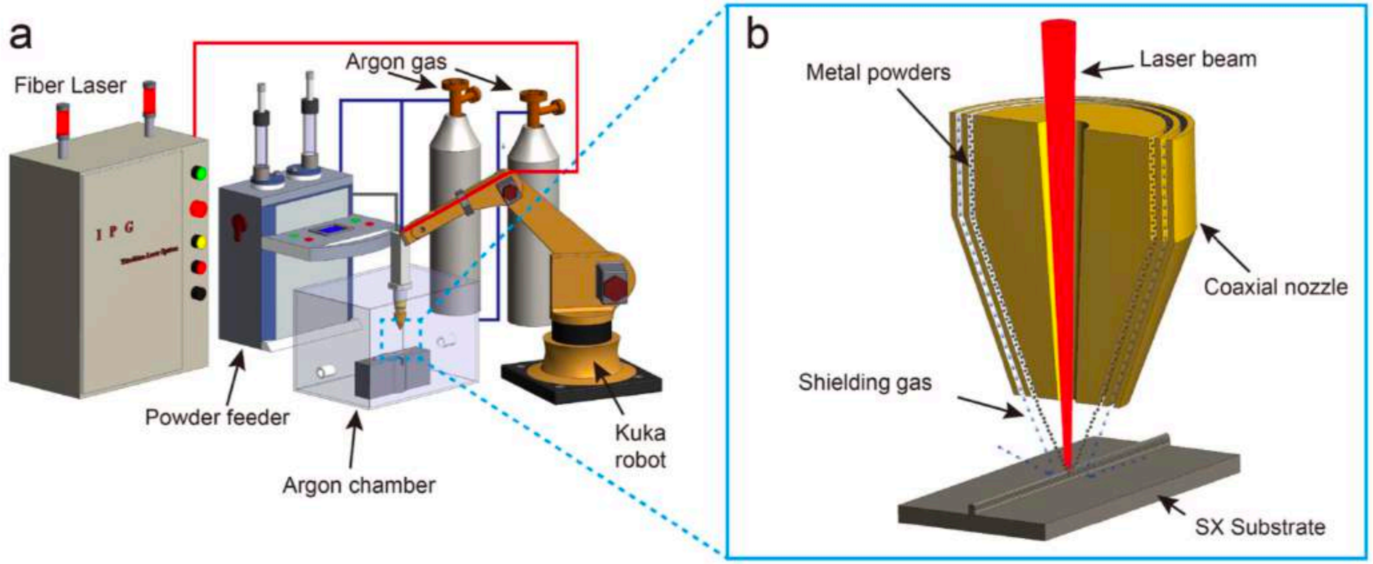

Fig. 1. (a) Directed energy deposition (DED) setup; (b) DED schematic diagram.

https://doi.org/10.1016/j.addma.2020.101228

Hot cracking behavior and mechanism of a third-generation Ni-based single- crystal superalloy during directed energy deposition

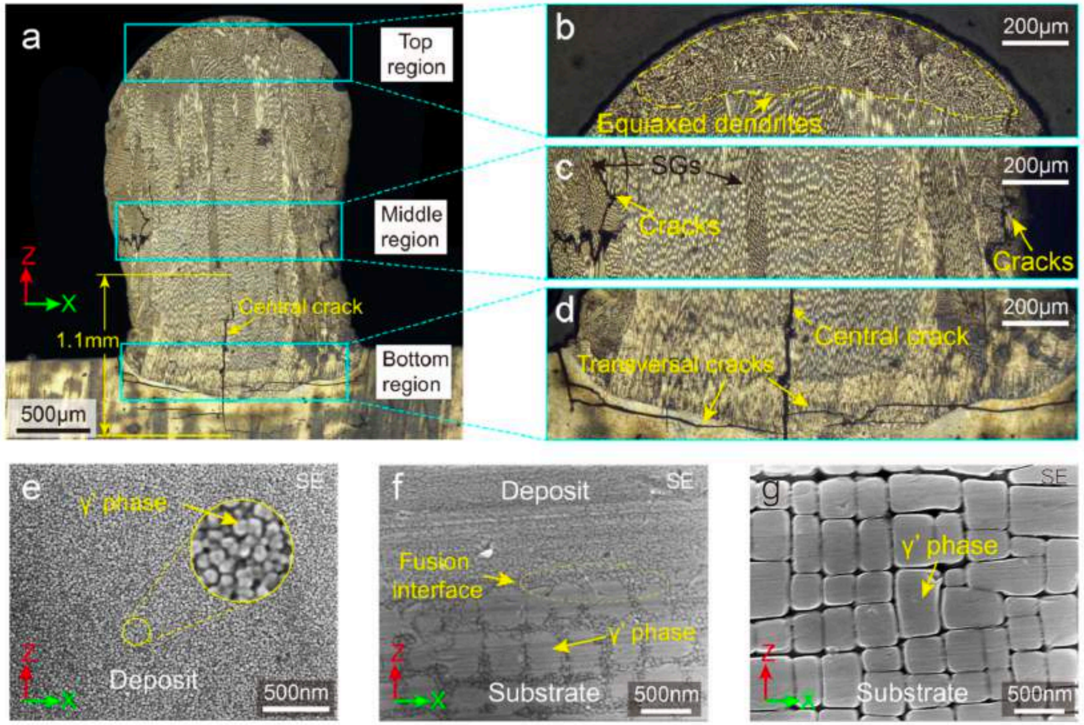

Fig. 4. OM images showing the microstructures of CMSX-10 on Ni-based SX superalloys (a); local enlargement microstructures of the top region (b), the middle region (c), and the bottom region (d) in the deposited specimen; the SE image of γ' precipitates in the deposit (e), near the fusion interface (f), and in the substrate (g).

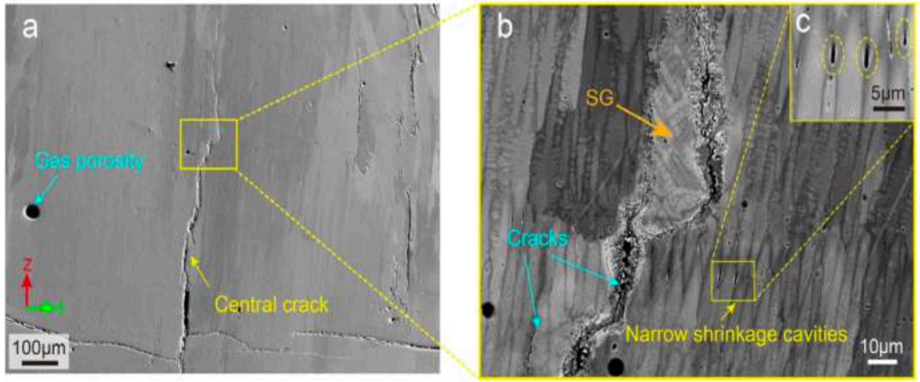

Fig. 6. Distribution of defects: (a) SE image of gas pores and cracks, (b) BSE images of strain grain (SG) and shrinkage cavities, (c) enlargement of shrinkage cavities.

https://doi.org/10.1016/j.addma.2020.101228

Hot cracking behavior and mechanism of a third-generation Ni-based single- crystal superalloy during directed energy deposition

Stray grains (**SGs**)

Low-angle grain boundaries (5°< **LAGBs** <15°)

Low-angle grain boundaries (**HAGBs**)

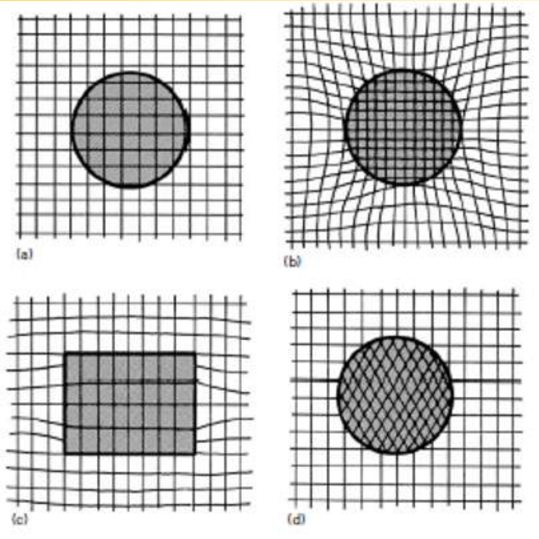

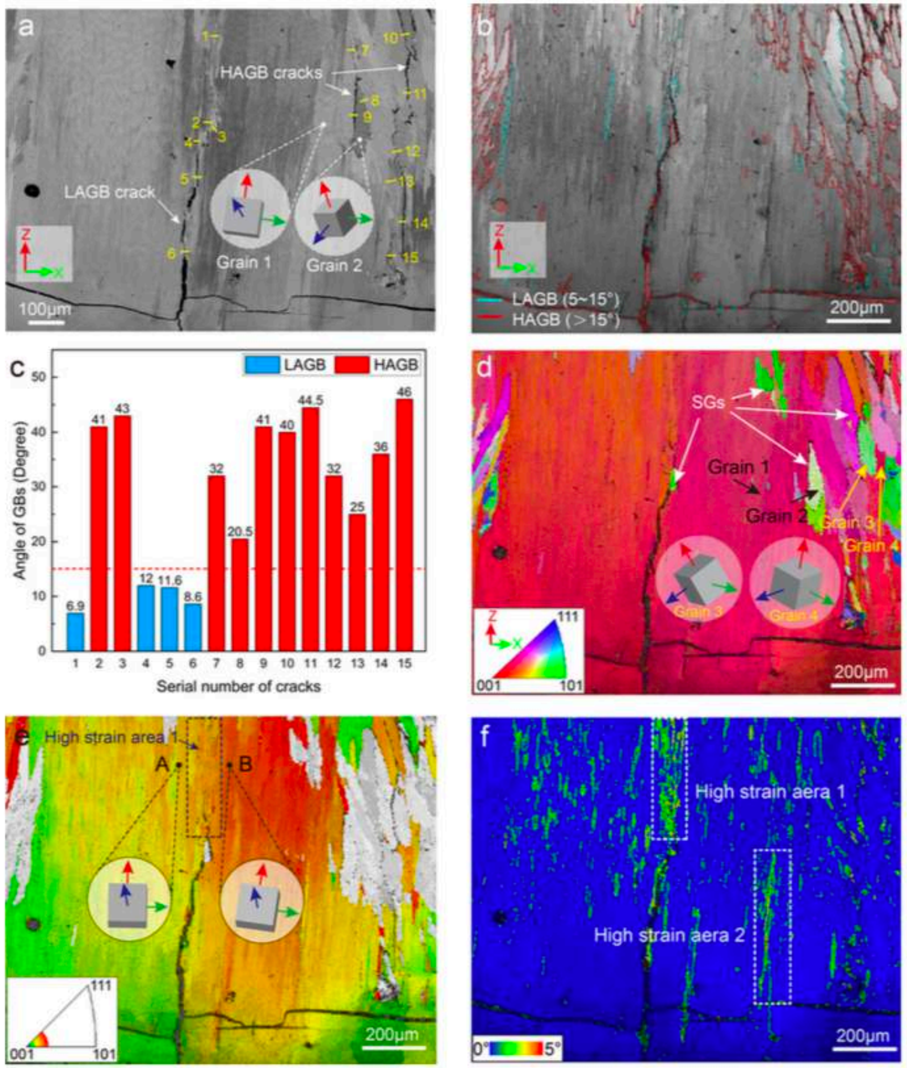

Fig. 7. (a) BSE image showing the distribution of fifteen cracks in the cross-section; (b) EBSD image showing the GB distribution map of HAGBs and LAGBs; (c) angles of the GBs corresponding to the fifteen cracks in a; (d) the inverse pole figure (IPF) along the Z direction of the cross-section in the X-Z plane; (e) crystal direction map compared with the original [001] direction; (f) KAM map showing the strain concentration.

https://doi.org/10.1016/j.addma.2020.101228

Hot cracking behavior and mechanism of a third-generation Ni-based single- crystal superalloy during directed energy deposition

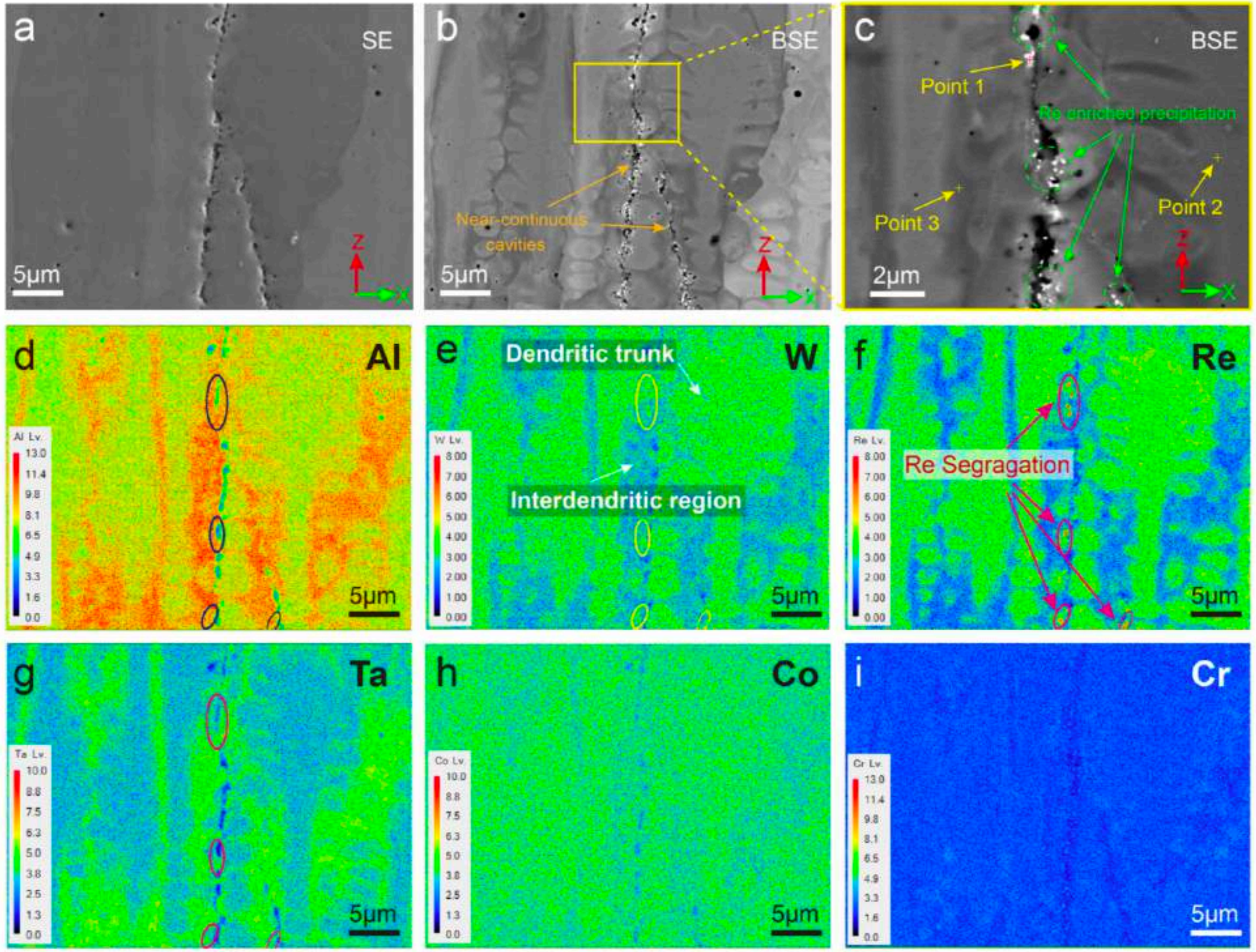

Fig. 8. EPMA elemental distributions of the region near the central crack. (a) SE image of the crack initiation; (b) BSE images of the crack initiation; (c) enlargement of the selected region in b; Elemental distribution maps of: (d) Al; (e) W; (f) Re; (g) Ta; (h) Co; (i) Cr.

https://doi.org/10.1016/j.addma.2020.101228

Damage and Failure analysis – microstructure heterogeneities stress intensifiers, nucleation and growth of cracks

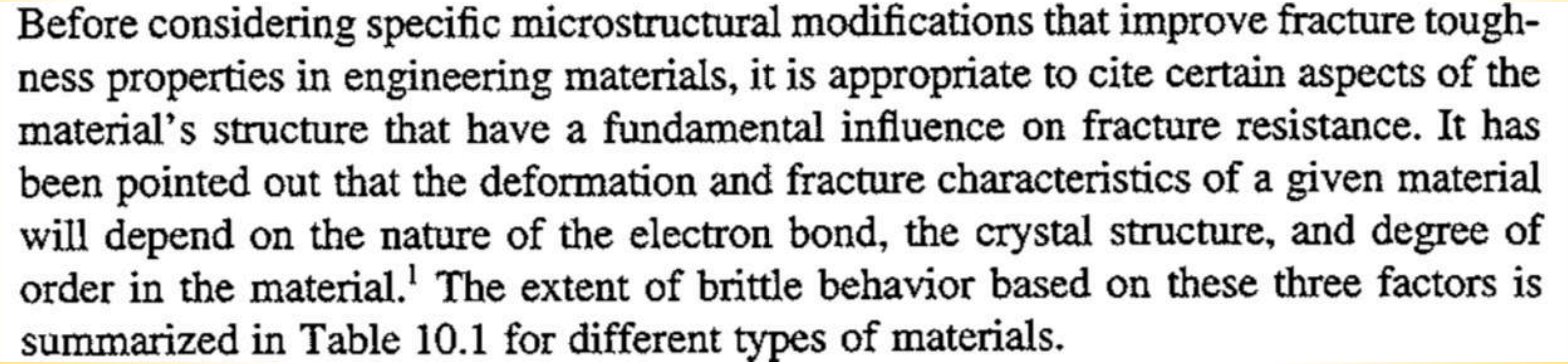

Before considering specific microstructural modifications that improve fracture toughness properties in engineering materials, it is appropriate to cite certain aspects of the material's structure that have a fundamental influence on fracture resistance. It has been pointed out that the deformation and fracture characteristics of a given material will depend on the nature of the electron bond, the crystal structure, and degree of order in the material.[1] The extent of brittle behavior based on these three factors is summarized in Table 10.1 for different types of materials.

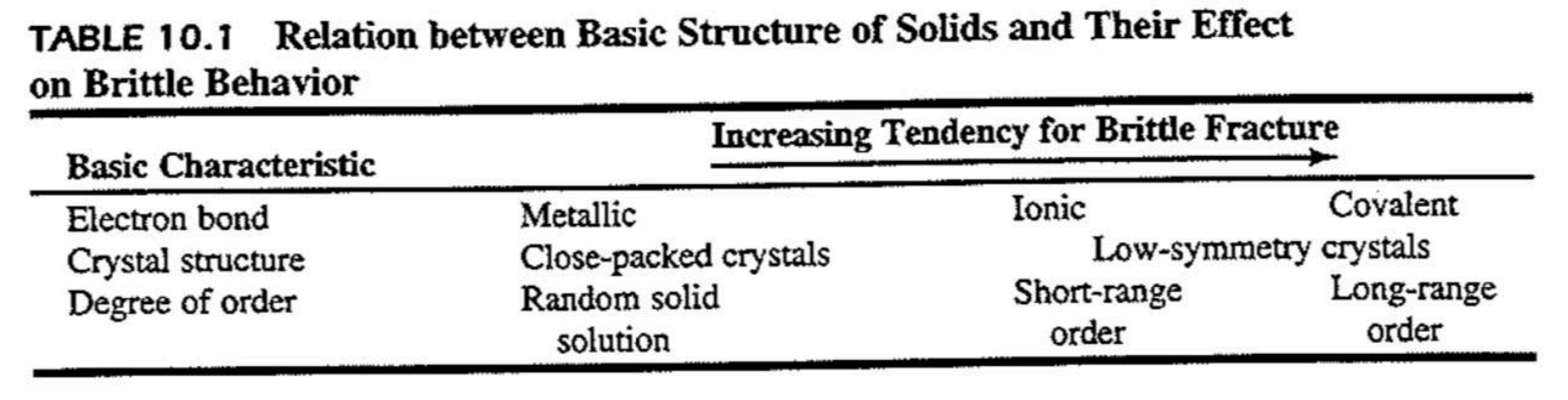

TABLE 10.1 Relation between Basic Structure of Solids and Their Effect on Brittle Behavior

Basic Characteristic	Increasing Tendency for Brittle Fracture →		
Electron bond	Metallic	Ionic	Covalent
Crystal structure	Close-packed crystals	Low-symmetry crystals	
Degree of order	Random solid solution	Short-range order	Long-range order

Short-range ordering (SRO)

The addition of a solute to a metal lattice will suppress the plastic flow whenever the resulting solid solution changes from that of a random distribution to that of short – range order and finally to long-range order.

The mechanical behavior of alloys is heavily influenced by the segregation of elements and atomic ordering within single-phase regions. Short-range ordering (SRO) describes the preferential local ordering of elements within a lattice, over spatial dimensions that are typically on the order of a few nearest neighbor spacings.

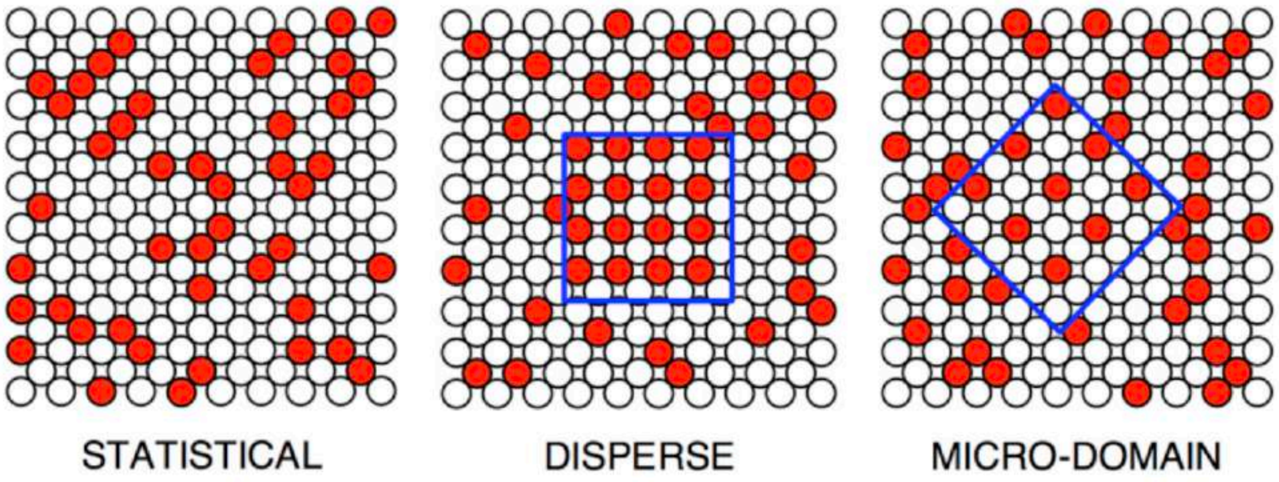

Fig. 1. Examples of the different types of short-range order that can be exhibited by a crystalline alloy system. In each case the average unit cell of each box is the same. In the disperse and micro-domain models, the ordered region is outlined.

https://advances.sciencemag.org/content/5/12/eaax2799

https://doi.org/10.1016/j.actamat.2016.05.031

long-range order

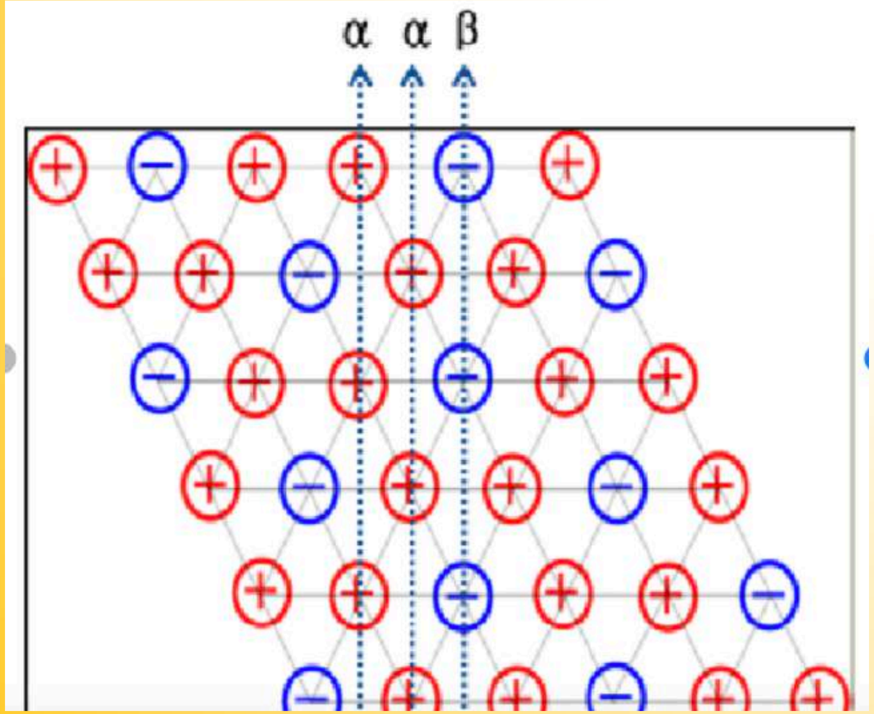

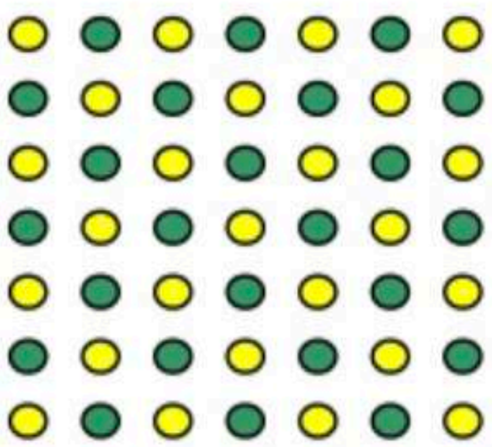

Long-range order (LRO):
Differentiation „η" of probalilities of particular sublattice sites being occupied by particular atoms.

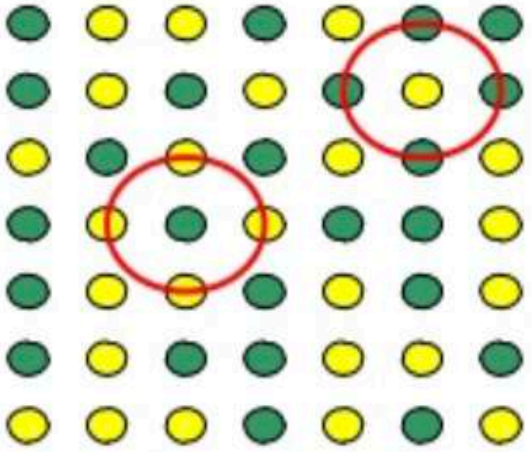

Short-range order (SRO):
Tendency for A-(B-) atoms to be preferencially surrounded by B- or A-atoms (correlation functions).

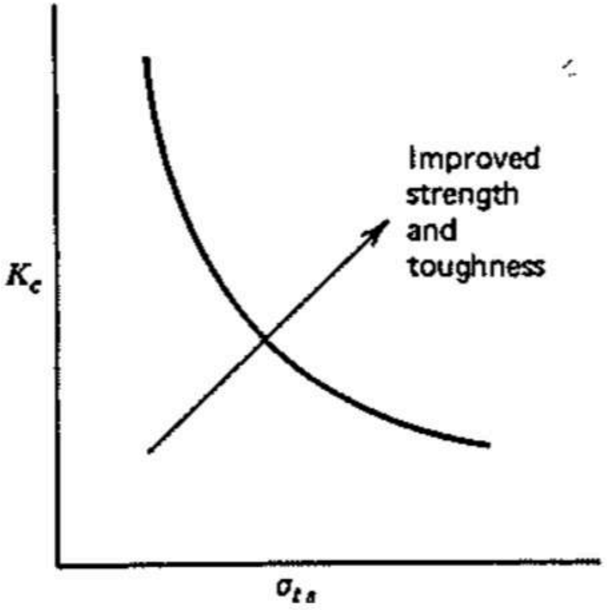

FIGURE 10.1 Inverse relation between fracture toughness and strength. Optimization of alloy properties would involve shifting curve in direction of the arrow.

1. Improved alloy chemistry and melting practice to remove or make innocuous undesirable tramp elements that degrade toughness.
2. Development of optimum microstructures and phase distributions to maximize toughness.
3. Microstructural refinement.

Anisotropy

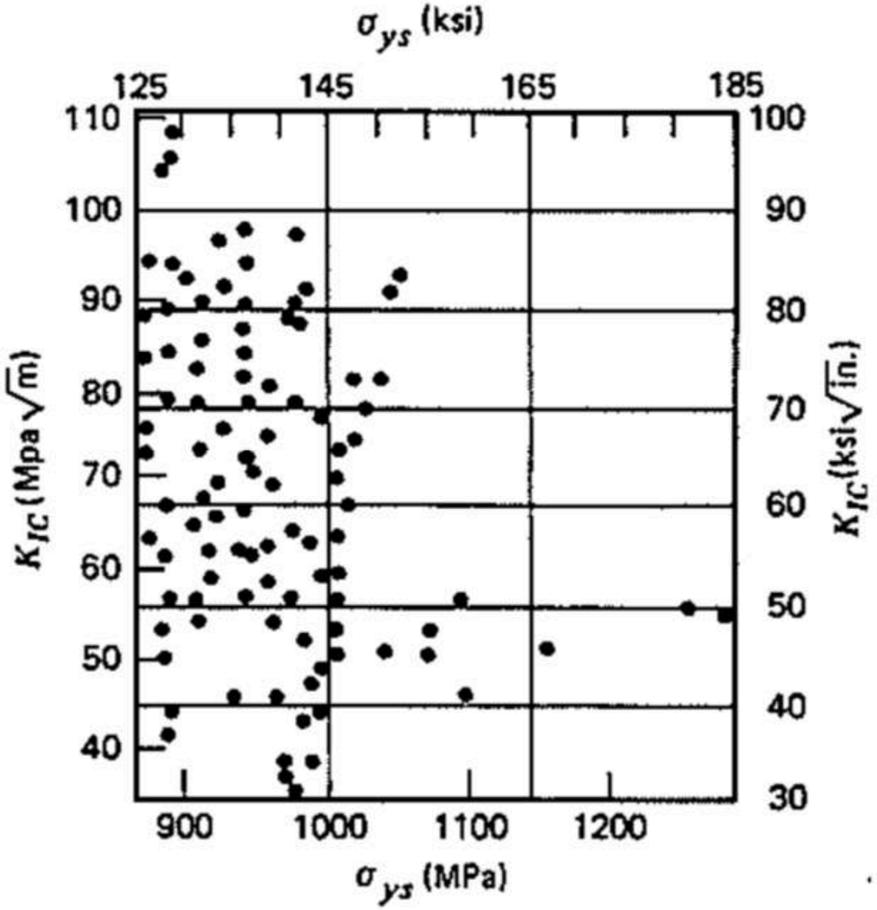

FIGURE 10.2 Fracture toughness data for Ti-6Al-4V alloy. Large scatter in experimental results suggests different microstructures present.[2] (From M. J. Harrigan, *Metals Engineering Quarterly*, May 1974, copyright American Society for Metals.)

Anisotropy

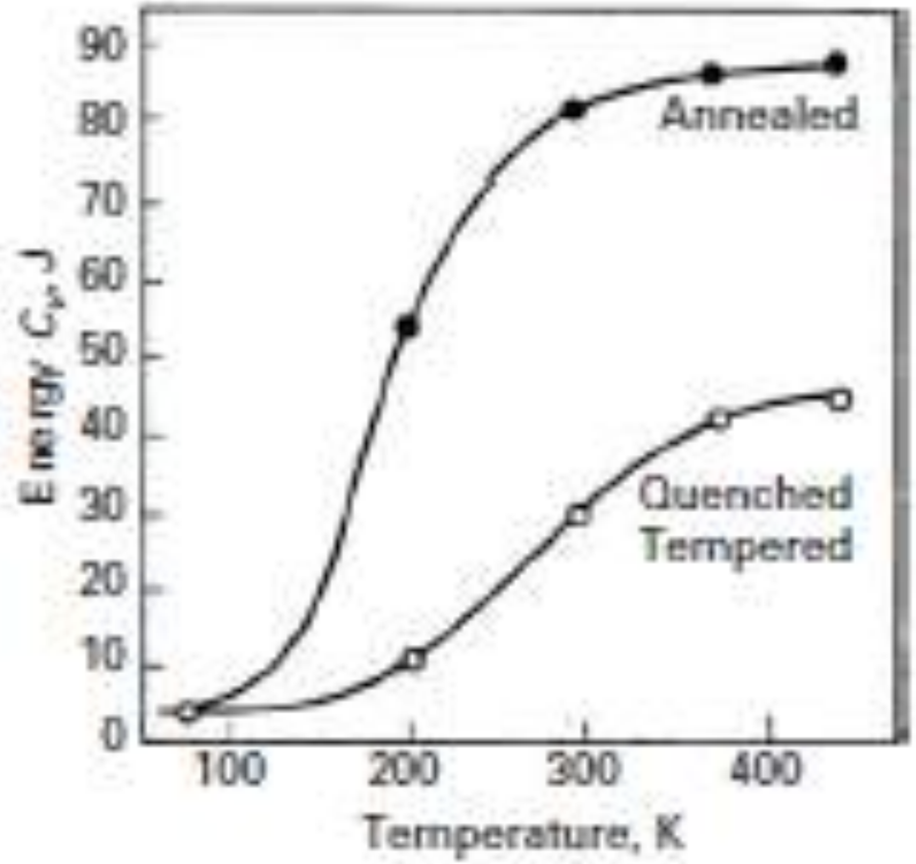

Fig. 9.2 Energy absorbed versus temperature for a steel in annealed and in quenched and tempered states. (Adapted with permission from J. C. Miguez Suarez and K. K. Chawla, *Metalurgia-ABM*, 34 (1978) 825.)

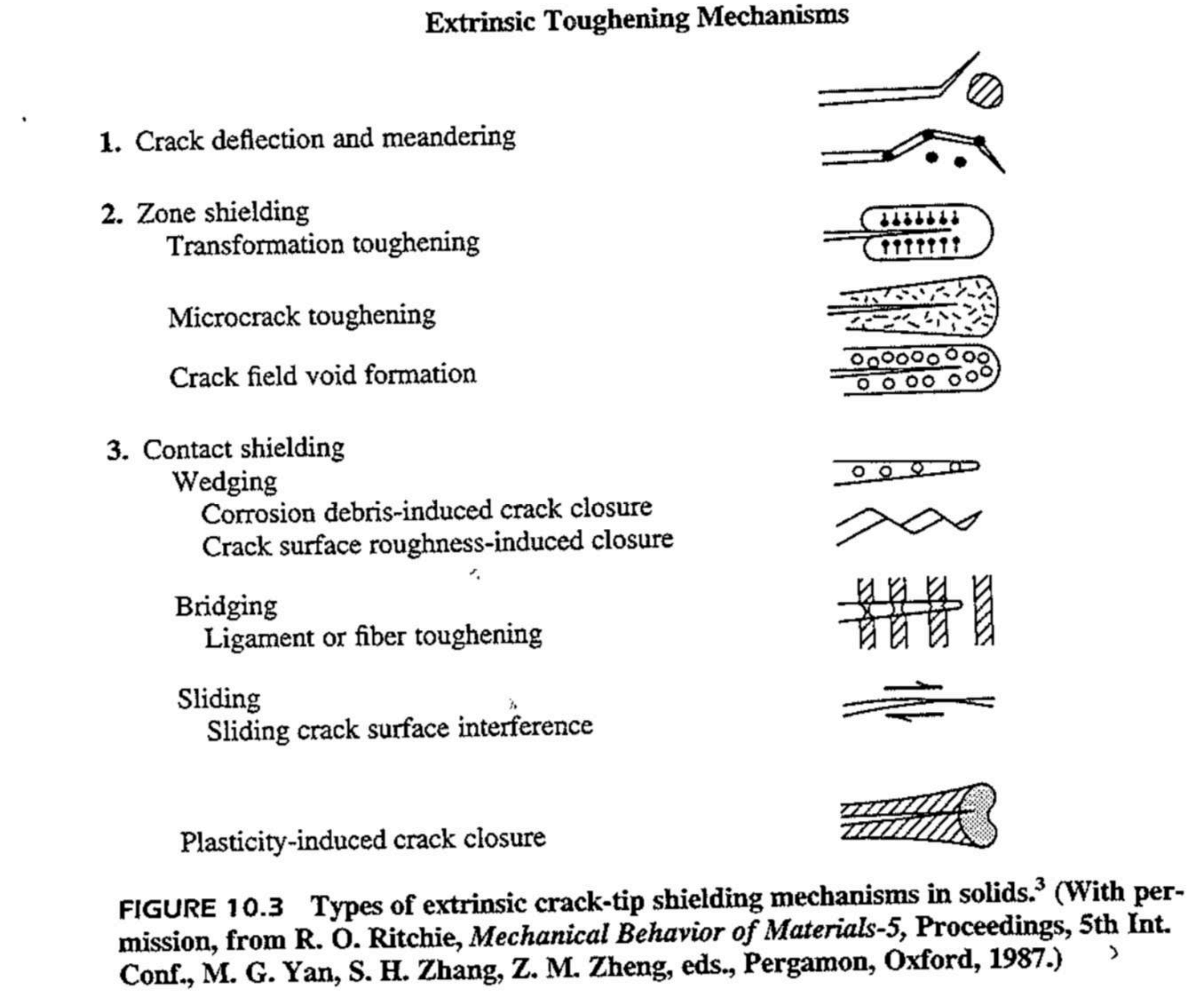

Extrinsic Toughening Mechanisms

1. Crack deflection and meandering

2. Zone shielding
   - Transformation toughening
   - Microcrack toughening
   - Crack field void formation

3. Contact shielding
   - Wedging
     - Corrosion debris-induced crack closure
     - Crack surface roughness-induced closure
   - Bridging
     - Ligament or fiber toughening
   - Sliding
     - Sliding crack surface interference
   - Plasticity-induced crack closure

FIGURE 10.3 Types of extrinsic crack-tip shielding mechanisms in solids.[3] (With permission, from R. O. Ritchie, *Mechanical Behavior of Materials-5*, Proceedings, 5th Int. Conf., M. G. Yan, S. H. Zhang, Z. M. Zheng, eds., Pergamon, Oxford, 1987.)

Fig. 8.27 Some toughening mechanisms in ceramics.

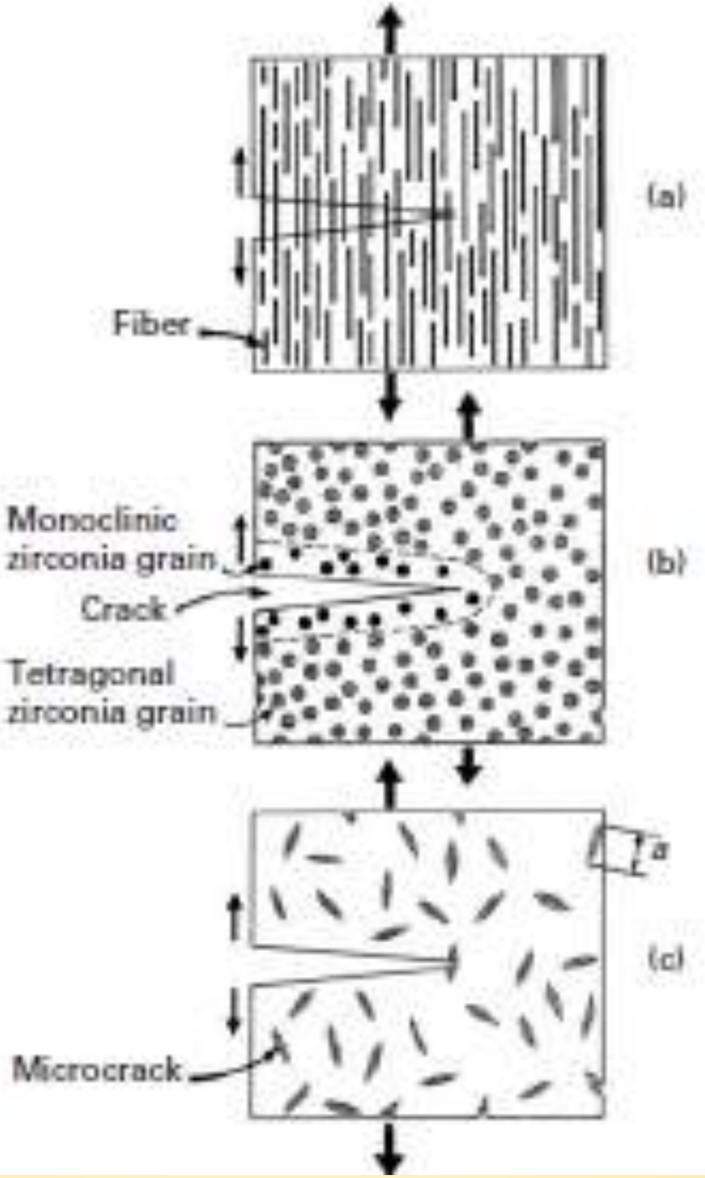

Anisotropy

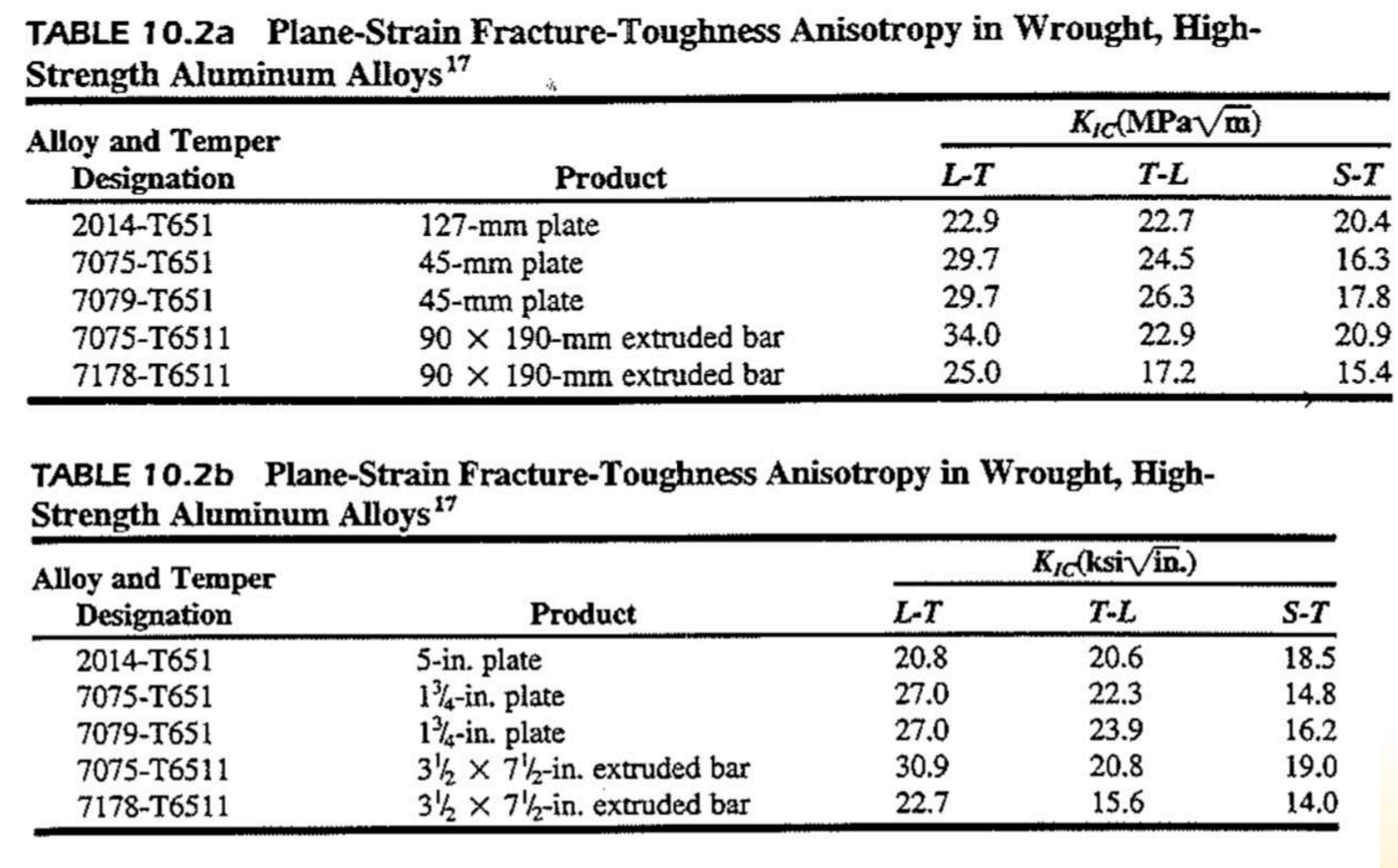

TABLE 10.2a Plane-Strain Fracture-Toughness Anisotropy in Wrought, High-Strength Aluminum Alloys[17]

Alloy and Temper Designation	Product	K_{IC}(MPa$\sqrt{m}$) L-T	K_{IC}(MPa$\sqrt{m}$) T-L	K_{IC}(MPa$\sqrt{m}$) S-T
2014-T651	127-mm plate	22.9	22.7	20.4
7075-T651	45-mm plate	29.7	24.5	16.3
7079-T651	45-mm plate	29.7	26.3	17.8
7075-T6511	90 × 190-mm extruded bar	34.0	22.9	20.9
7178-T6511	90 × 190-mm extruded bar	25.0	17.2	15.4

TABLE 10.2b Plane-Strain Fracture-Toughness Anisotropy in Wrought, High-Strength Aluminum Alloys[17]

Alloy and Temper Designation	Product	K_{IC}(ksi$\sqrt{in.}$) L-T	K_{IC}(ksi$\sqrt{in.}$) T-L	K_{IC}(ksi$\sqrt{in.}$) S-T
2014-T651	5-in. plate	20.8	20.6	18.5
7075-T651	$1\frac{3}{4}$-in. plate	27.0	22.3	14.8
7079-T651	$1\frac{3}{4}$-in. plate	27.0	23.9	16.2
7075-T6511	$3\frac{1}{2} \times 7\frac{1}{2}$-in. extruded bar	30.9	20.8	19.0
7178-T6511	$3\frac{1}{2} \times 7\frac{1}{2}$-in. extruded bar	22.7	15.6	14.0

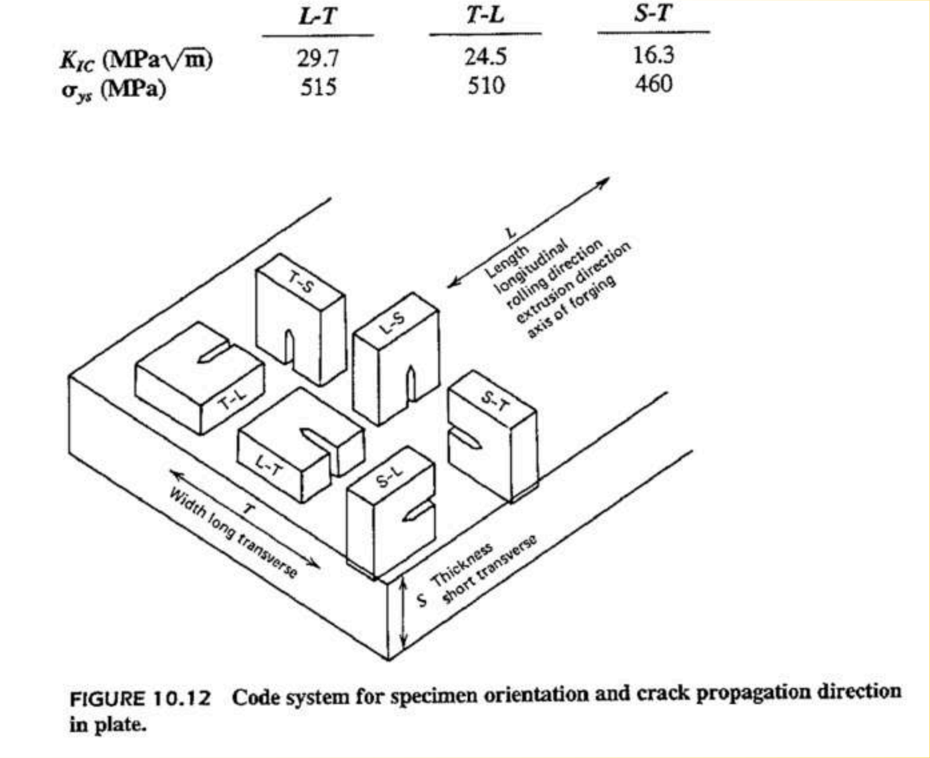

	L-T	T-L	S-T
K_{IC} (MPa$\sqrt{m}$)	29.7	24.5	16.3
σ_{ys} (MPa)	515	510	460

FIGURE 10.12 Code system for specimen orientation and crack propagation direction in plate.

Anisotropy

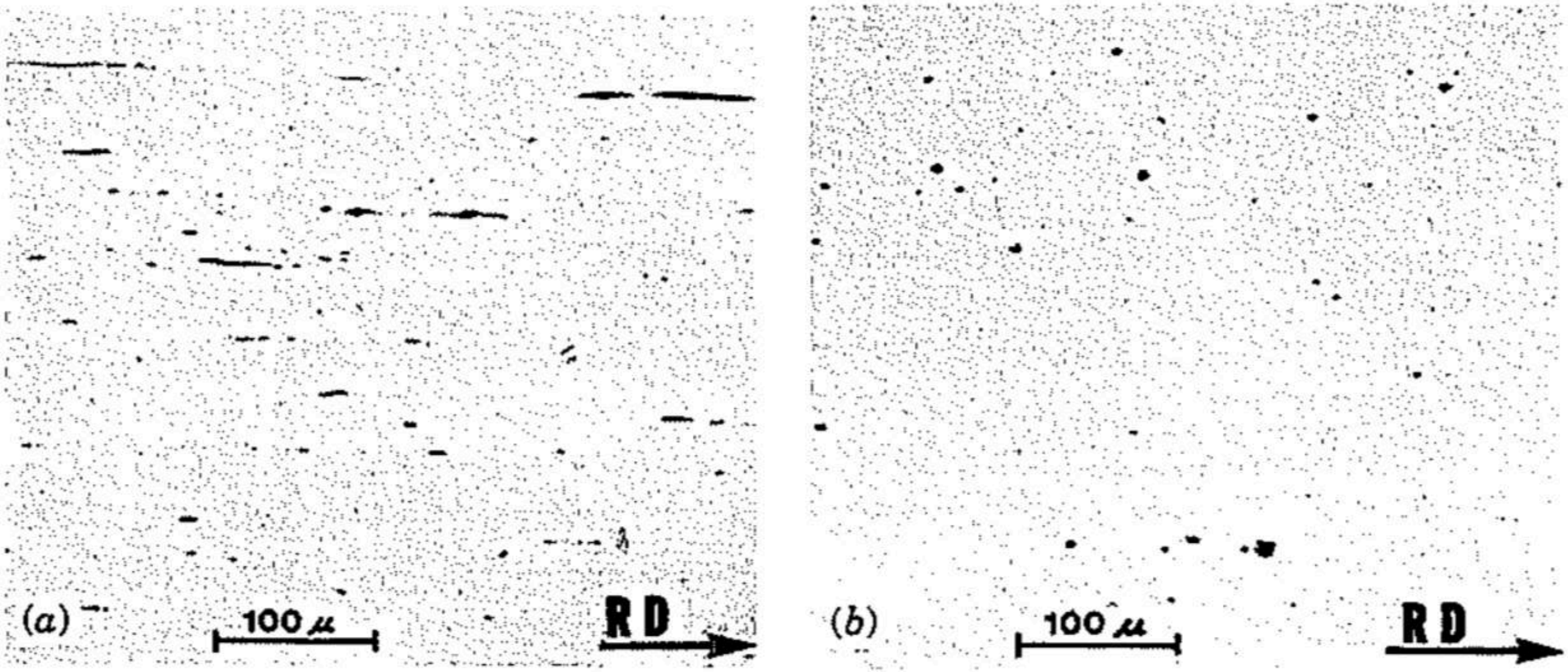

FIGURE 10.17 Longitudinal sections shown: (*a*) elongated manganese sulfide inclusions in quenched and tempered steel without inclusion shape control; (*b*) globular rare earth inclusions found in hot-rolled, low-alloy steel with inclusion shape control.

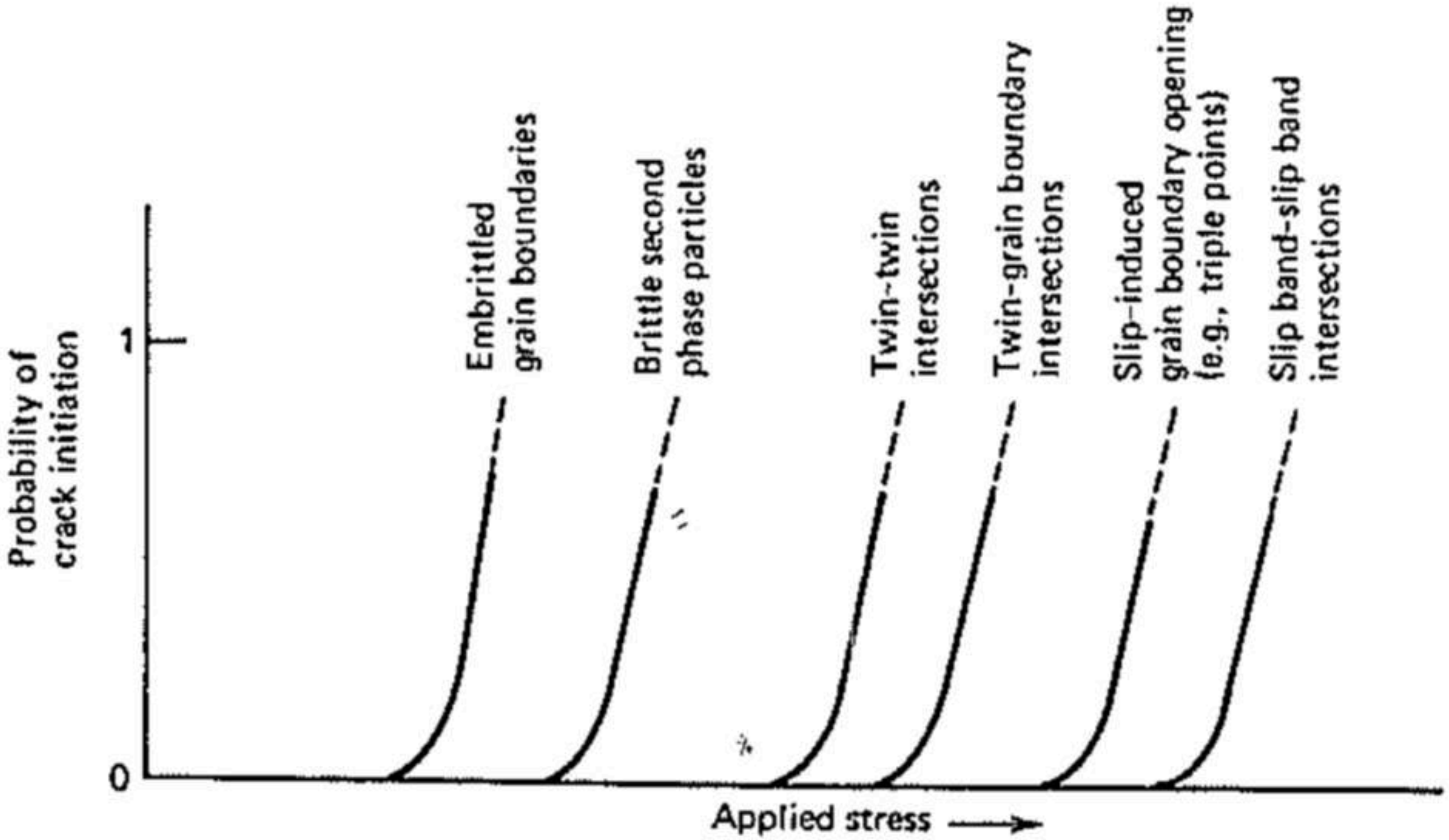

FIGURE 10.19 Probability as a function of applied stress that a particular microcrack formation mechanism will be operative.[25] (Reprinted with permission of Plenum Publishing Corporation, from C. J. McMahon, *Fundamental Phenomena in the Materials Sciences*, Vol. 4, 1967, p. 247.)

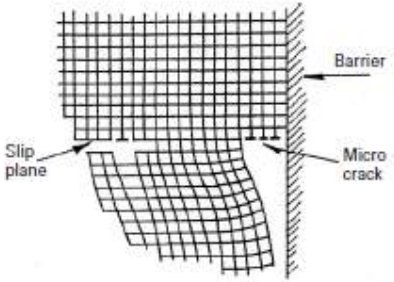

Fig. 8.3 Grouping of dislocations piled up at a barrier and leading to the formation of a microcrack (Zener–Stroh crack).

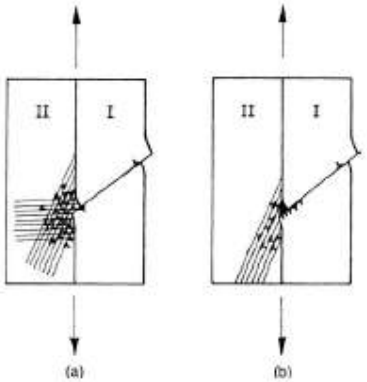

Fig. 8.4 Bicrystal with a slip band in grain I. (a) The stress concentration at the boundary of the barrier due to slip band is fully relaxed by multiple slip. (b) The stress concentration is only partially relaxed, resulting in a crack at the boundary.

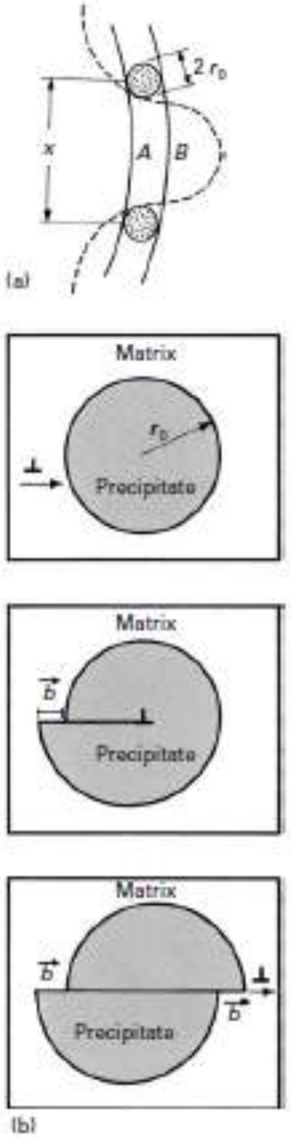

Fig. 10.21 (a) Dislocation at two successive positions A and B. (b) Dislocation shearing precipitate.

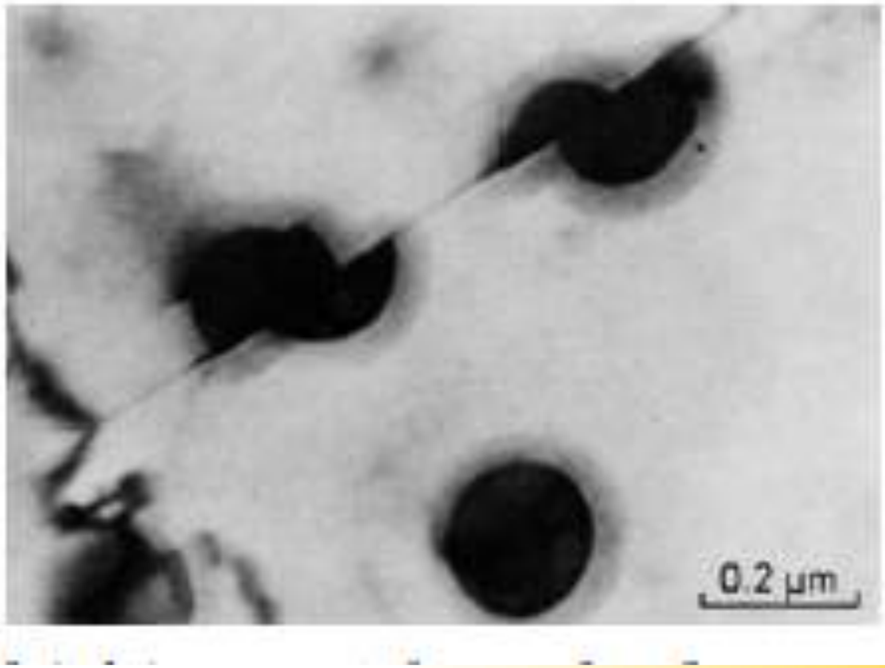

Fig. 10.20 γ′-precipitate particles sheared by dislocations in a Ni–19% Cr–69% Al alloy aged at 750 °C for 540 hours and strained 2%. The arrows indicate the two slip-plane traces (transmission electron microscopy) (Courtesy of H. Gleiter.)

Fig. 10.15 Different crystallographic relationships between matrix and second phase. (a) Complete coherency. (b) Coherency with strained, but continuous, lattice planes across the boundary. (c) Semicoherent, partial continuity of lattice planes across the interface. (d) Incoherent equilibrium precipitate, θ; no continuity of lattice planes across the interface.

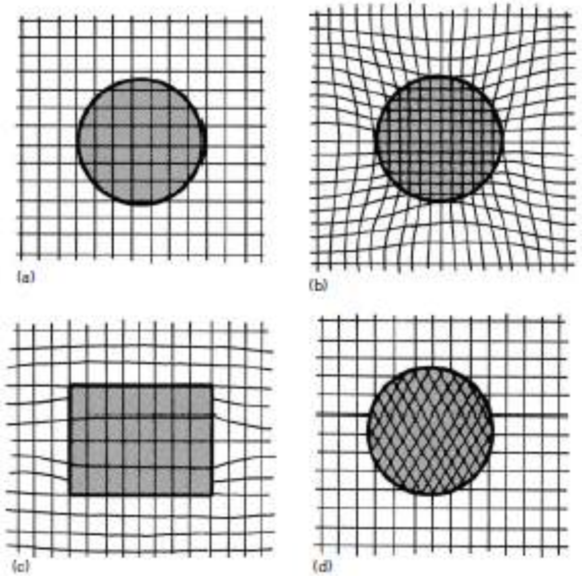

Fig. 10.16 Interfacial dislocations formed in a semicoherent precipitate. (From G. C. Weatherly and R. B. Nicholson, *Phil. Mag.*, 17 (1968), 801.)

Fig. 8.11 Nucleation of a cavity at a second-phase particle in a ductile material. (Adapted with permission from B. R. Lawn and T. R. Wilshaw, *Fracture of Brittle Solids* (Cambridge: Cambridge University Press, 1975), p. 40.)

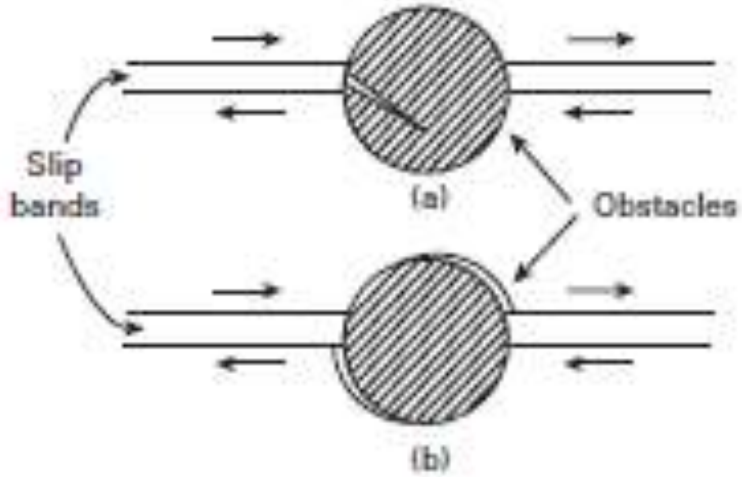

Fundamental Mechanisms Responsible for Creep

Diffusion Creep ($\sigma/G < 10^{-4}$)

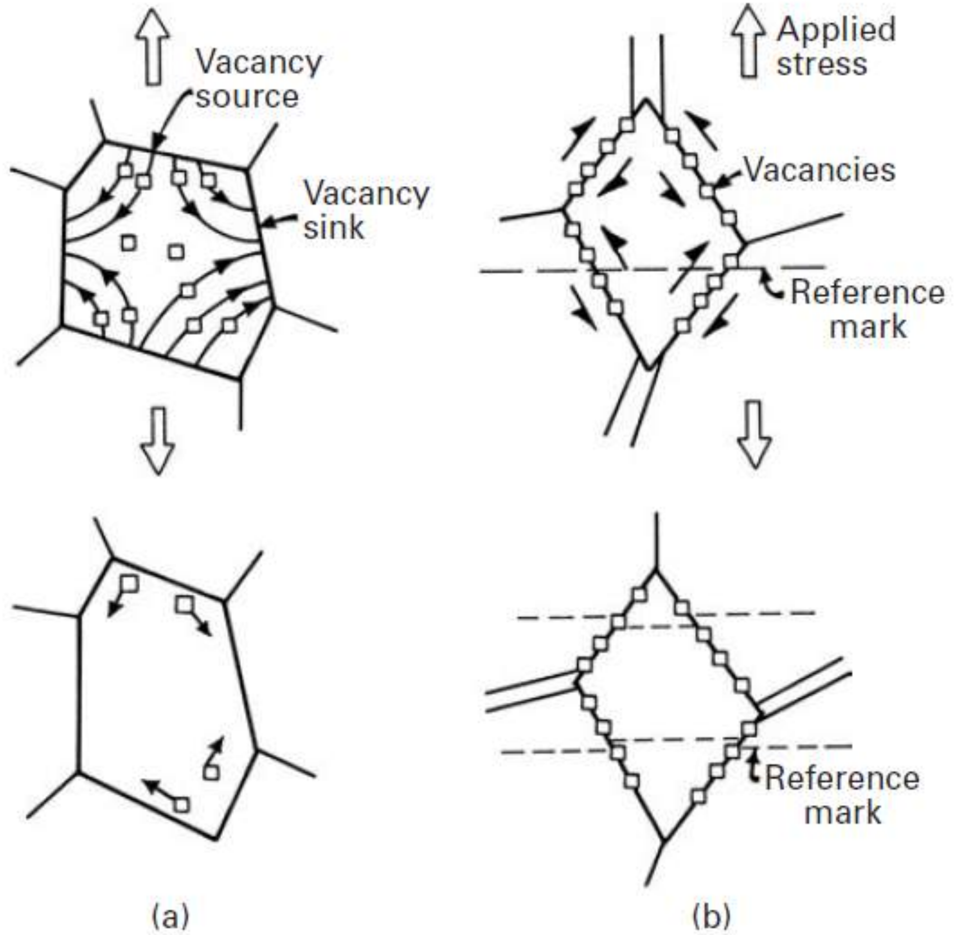

Fig. 13.11 Flow of vacancies according to (a) Nabarro–Herring and (b) Coble mechanisms, resulting in an increase in the length of the specimen.

Fundamental Mechanisms Responsible for Creep

Diffusion Creep ($\sigma / G < 10^{-4}$)

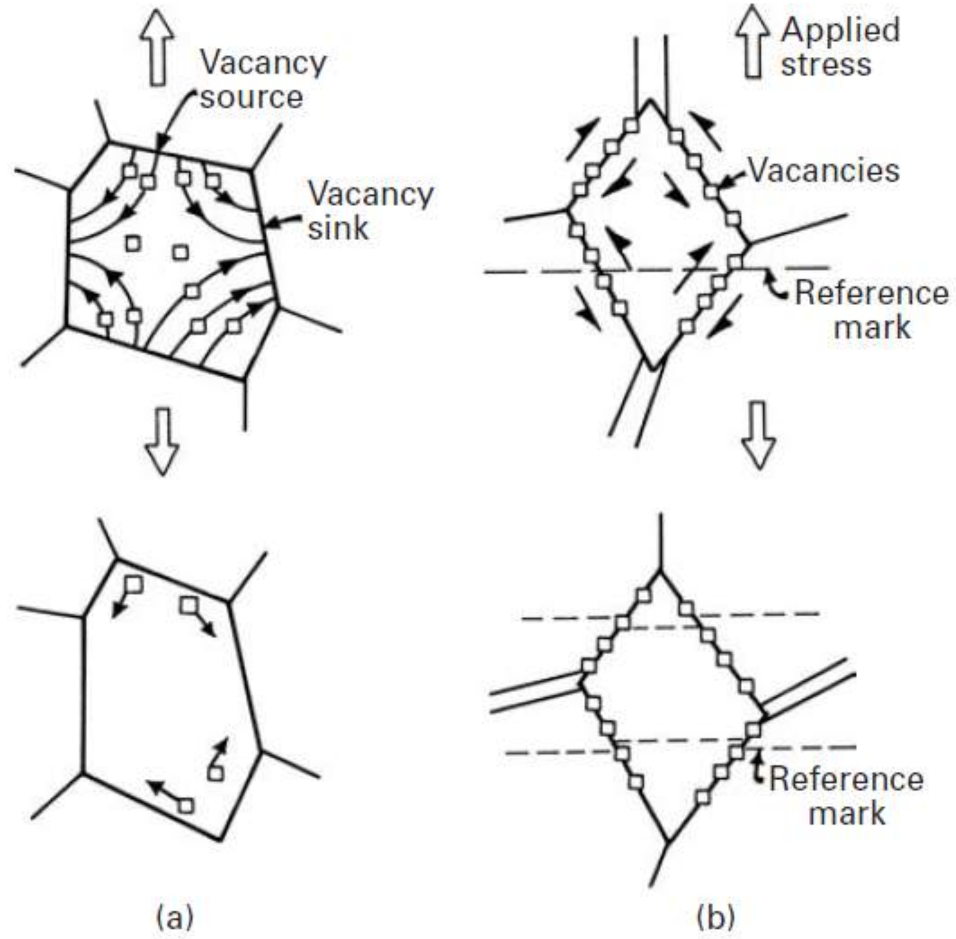

Fig. 13.11 Flow of vacancies according to (a) Nabarro–Herring and (b) Coble mechanisms, resulting in an increase in the length of the specimen.

Fundamental Mechanisms Responsible for Creep

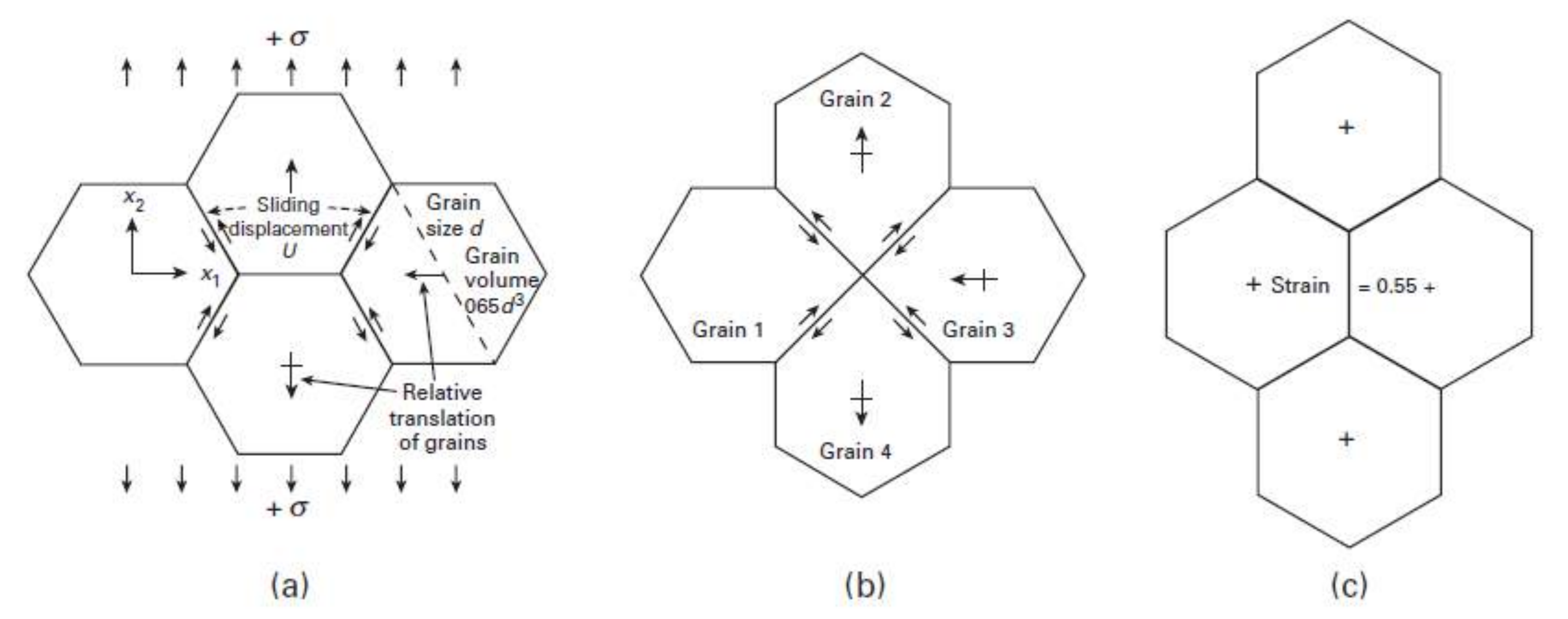

Fig. 13.19 Grain-boundary sliding assisted by diffusion in Ashby–Verrall's model. (Reprinted with permission from M. F. Ashby and R. A. Verrall, *Acta Met.*, 21 (1973) 149.)

Damage

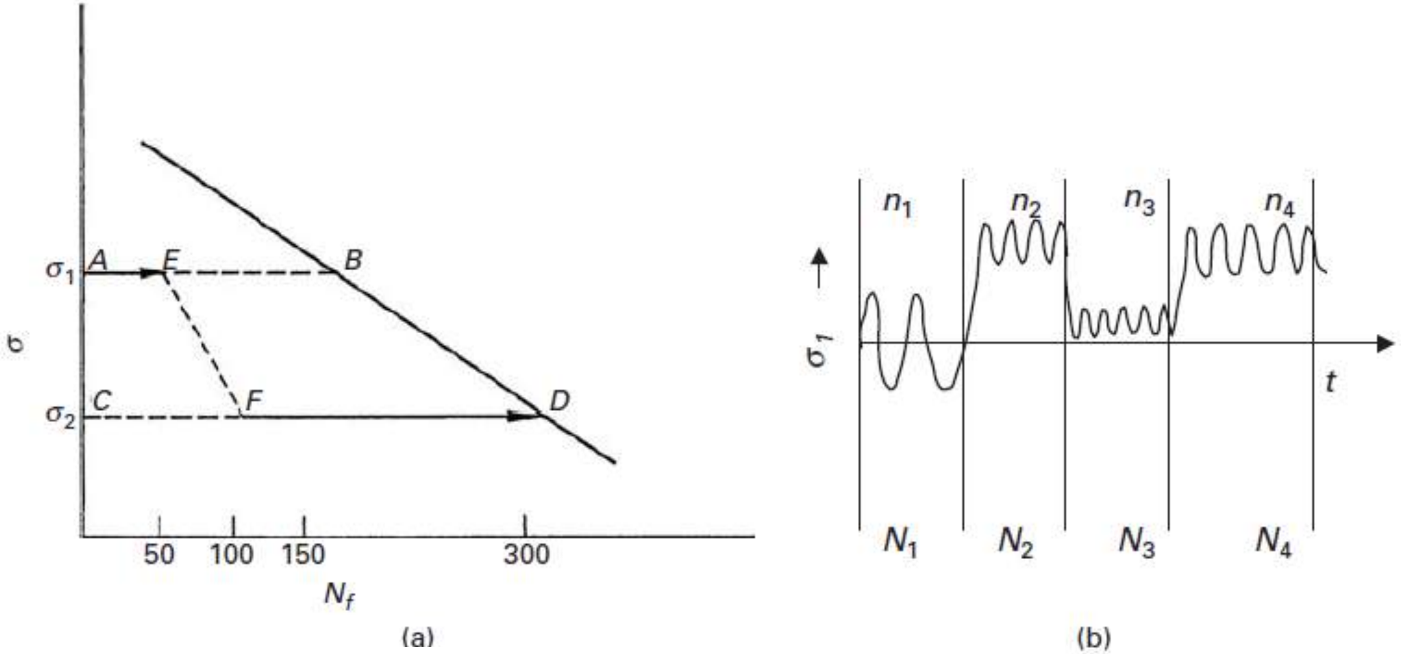

Fig. 14.10 (a) Damage accumulation, in a high-to-low loading sequence. (Adapted with permission from B. I. Sandor, *Fundamentals of Cyclic Stress and Strain* (Madison, WI: University of Wisconsin Press, 1972.)) (b) Sequence of block loadings at four different mean stresses and amplitudes.

Fig. 14.11 (a) Persistent slip bands in vein structure. Polycrystalline copper fatigued at a total strain amplitude of 6.4×10^{-4} for 3×10^5 cycles. Fatiguing carried out in reverse bending at room temperature and at a frequency of 17 Hz. The thin foil was taken 73 μm below the surface. (Courtesy of J. R. Weertman and H. Shirai.) (b) Cyclic shear stress, τ, vs. plastic cyclic shear strain, γ_{pl}, curve for a single crystal of copper oriented for single slip. (After H. Mughrabi, *Mater. Sci. Eng.*, 33 (1978) 207.) The terms $\gamma_{pl,\,M}$ and $\gamma_{pl,\,PSB}$ refer to cyclic plastic shear strain in the matrix and persistent slip bands, respectively. (c) Intrusions/extrusions in a tin-based solder due to thermal fatigue. (Courtesy of N. Chawla and R. Sidhur.)

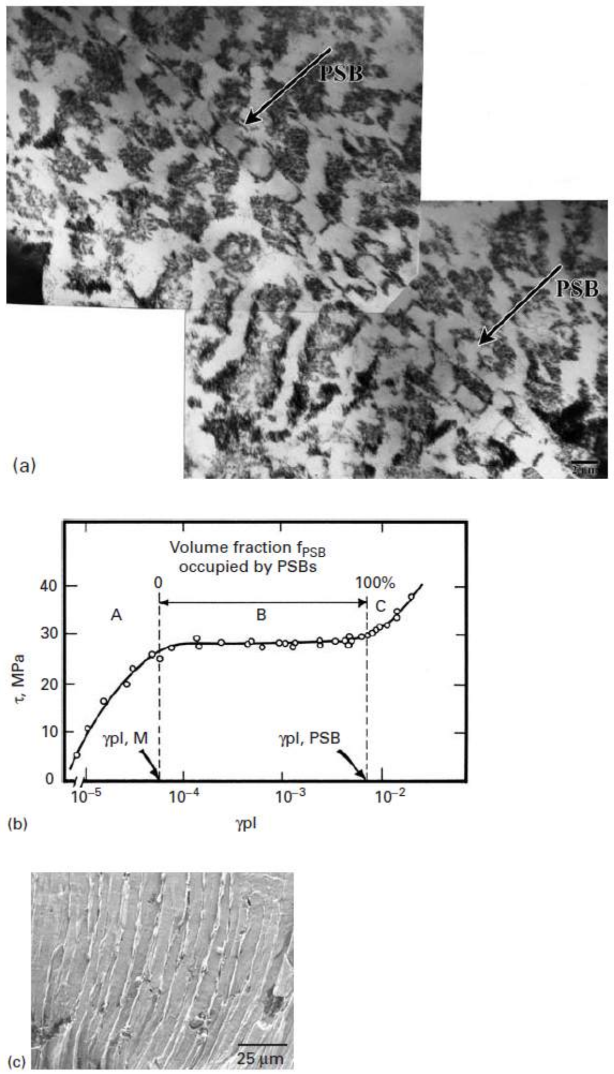

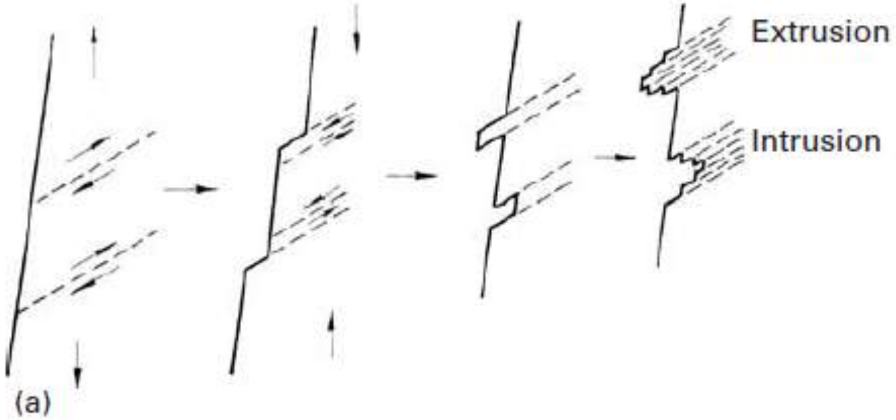

Fig. 14.13 (a) Fatigue crack nucleation at slip bands. (b) SEM of extrusions and intrusions in a copper sheet. (Courtesy of M. Judelwicz and B. Ilschner.)

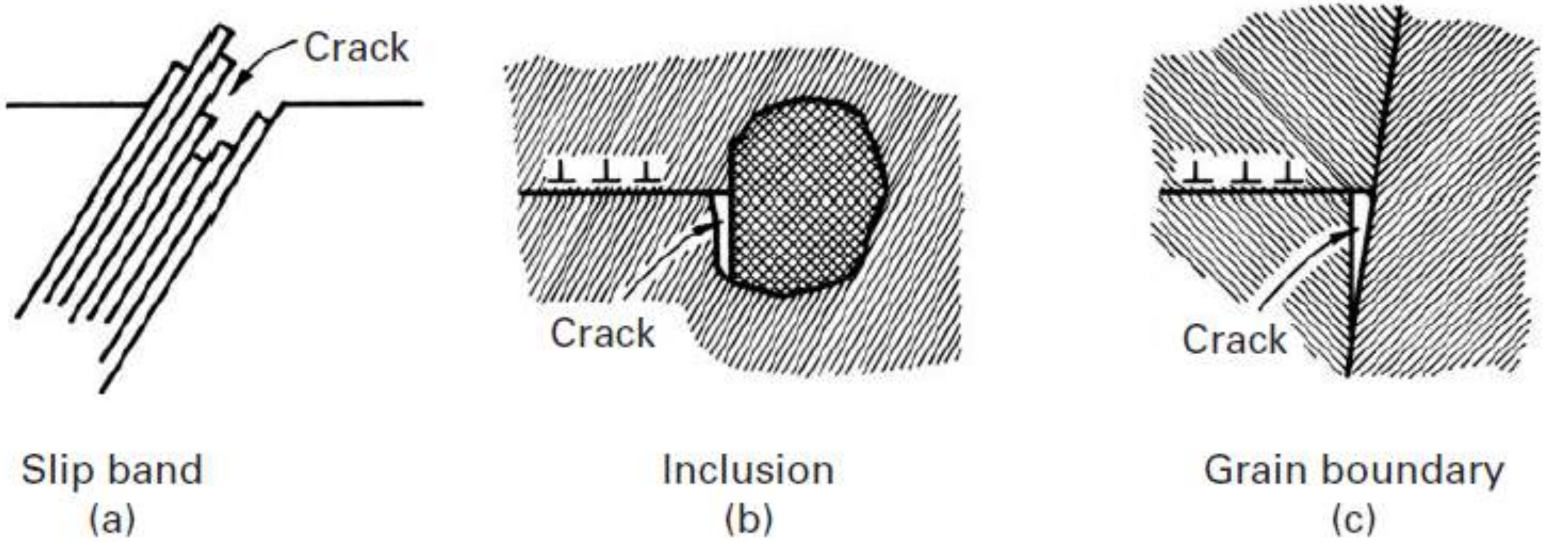

Fig. 14.14 Some mechanisms of fatigue crack nucleation. (After J. C. Grosskreutz, *Tech. Rep. AFML-TR-70–55* (Wright–Patterson AFB, OH: Air Force Materials Laboratory), 1970.)

Fig. 14.27 Intrinsic and extrinsic mechanisms of fatigue damage. (After R. O. Ritchie, *Intl. J. Fracture*, 100 (1999) 55.)

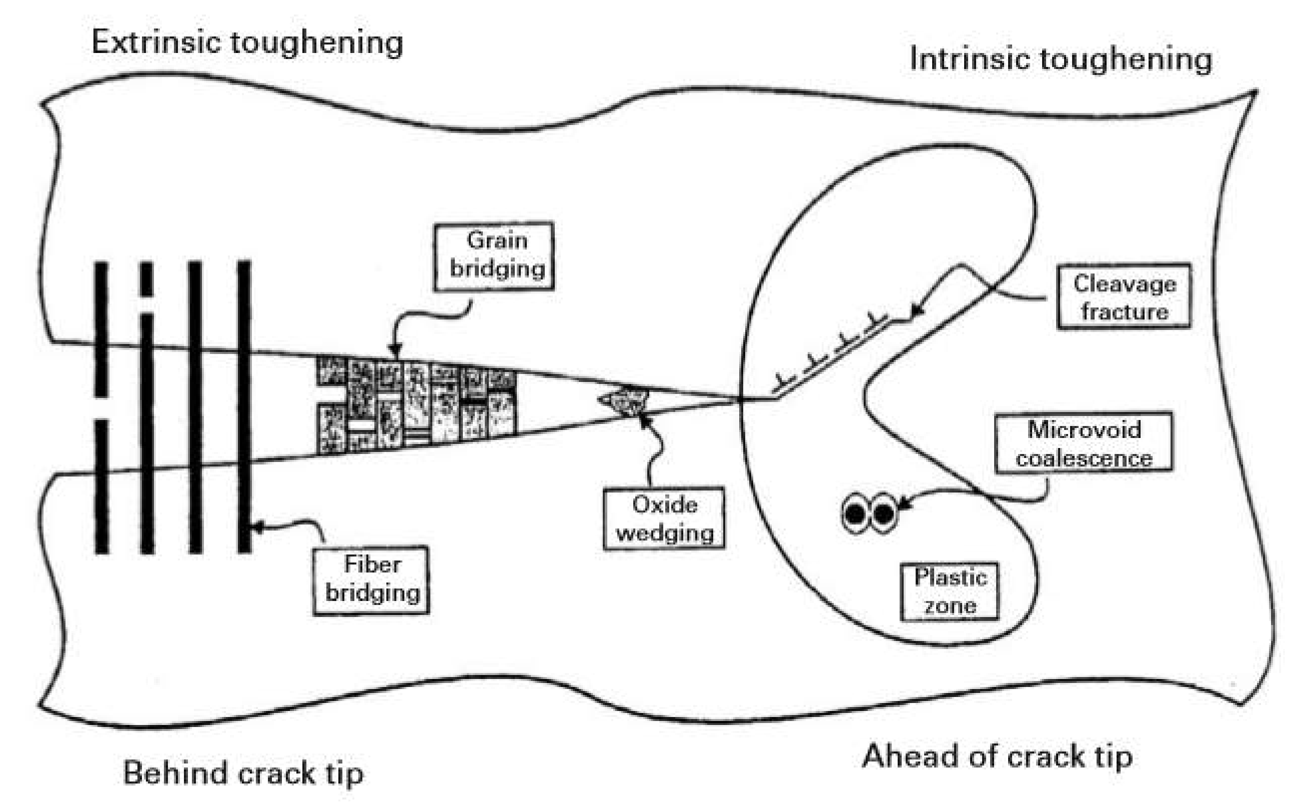

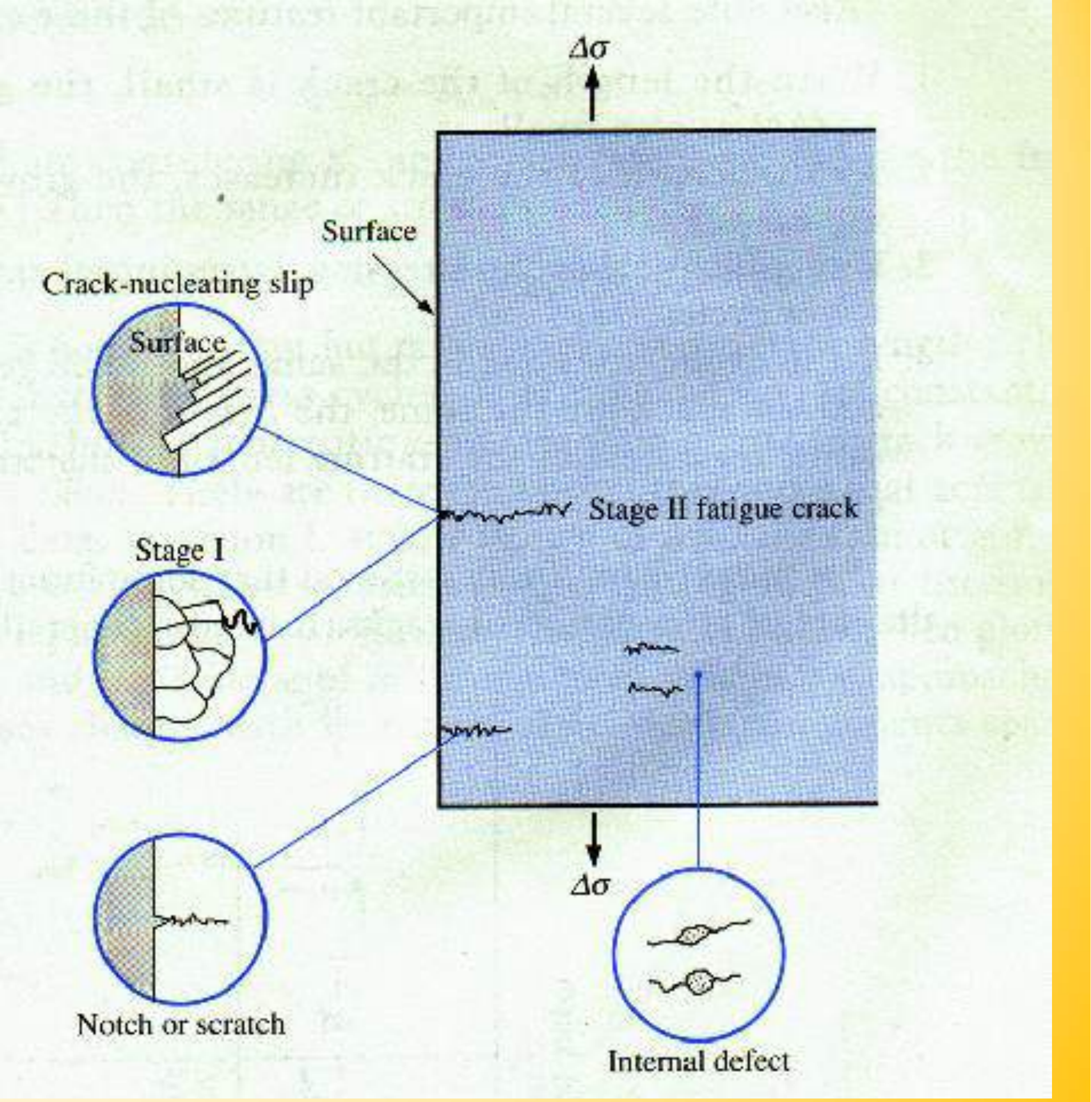

Fatigue Crack Propagation

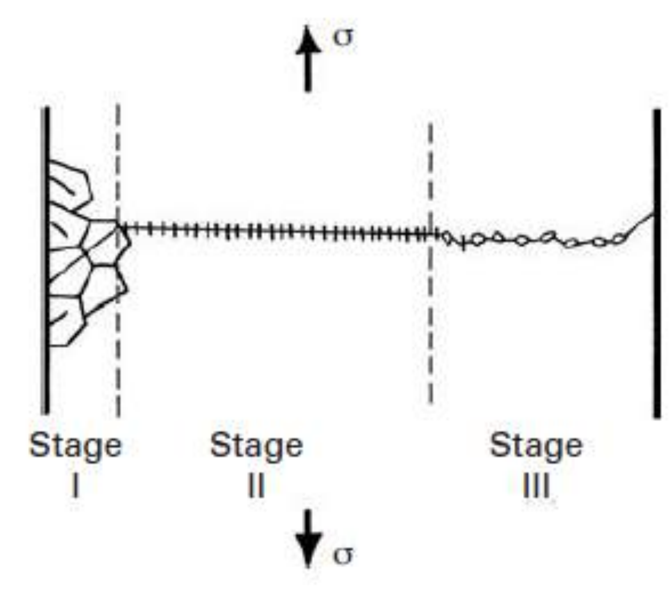

Fig. 14.16 Stages I, II, and III of fatigue crack propagation.

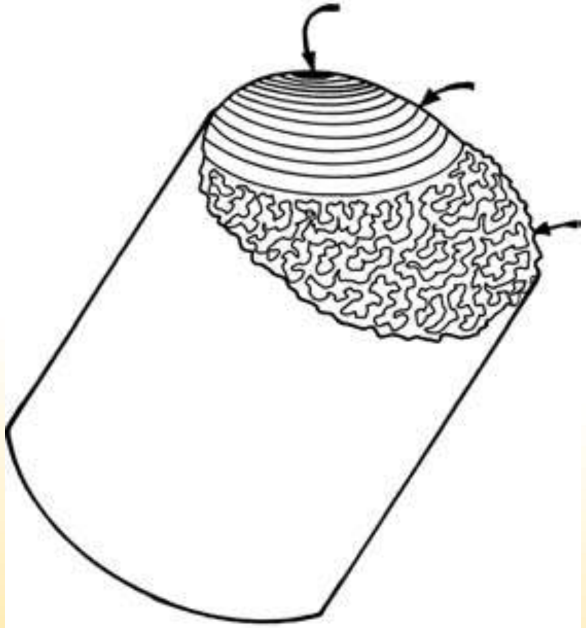

Wear

Microstructural parameters that influence the resistance are: the hardness, morphology, size, volume fraction and distribution of the second phase; and properties of the matrix and the matrix-precipitate interface.

Figure 9 - Effect of the relative hardness on the transition of abrasion regimes for single-phase and multiphase materials.

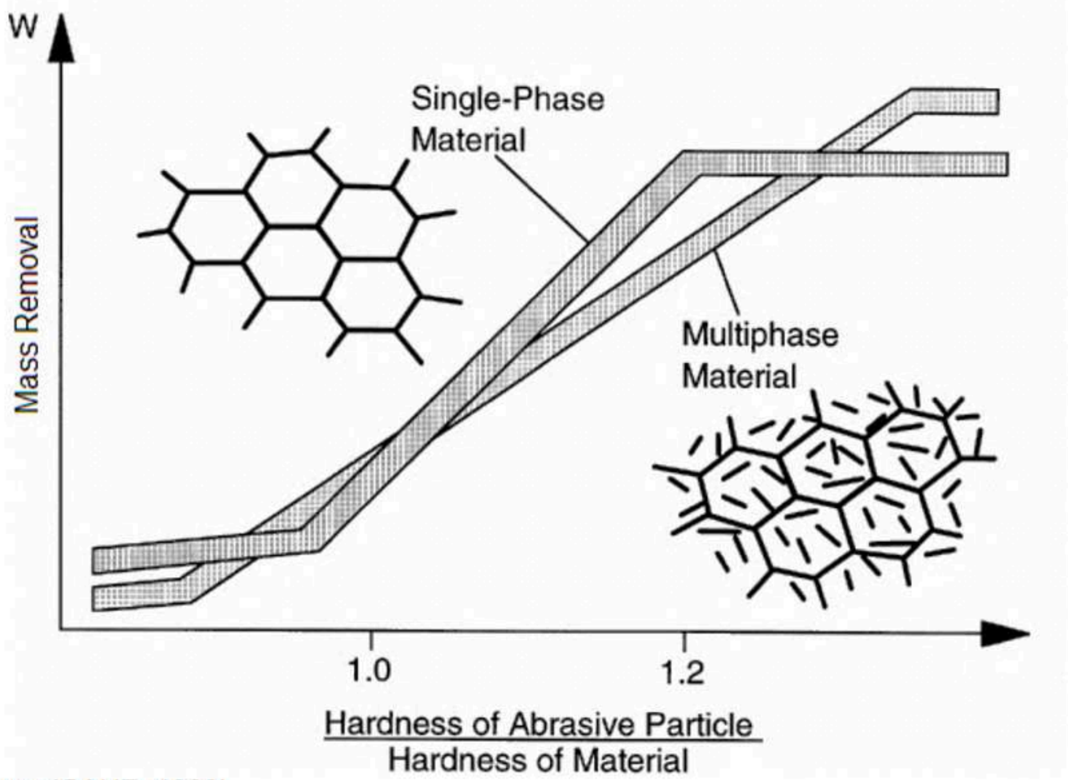

Reference: (GAHR, 1998).

Wear

(i-) hard precipitates lower than the width of the scratch track were pushed and removed with the chip formation; they did not act to enhance the material removal resistance;

(ii-) hard precipitates higher than the track width, considering constant normal load, tend to reduce the local depth of penetration and width; they were not easily removed, and they strongly acted on the material removal resistance.

Numerical simulation by FEM of scratch tests: von Mises stress fields that allow analysing the effect of the size of second phase particles when compared to the abrasive size.

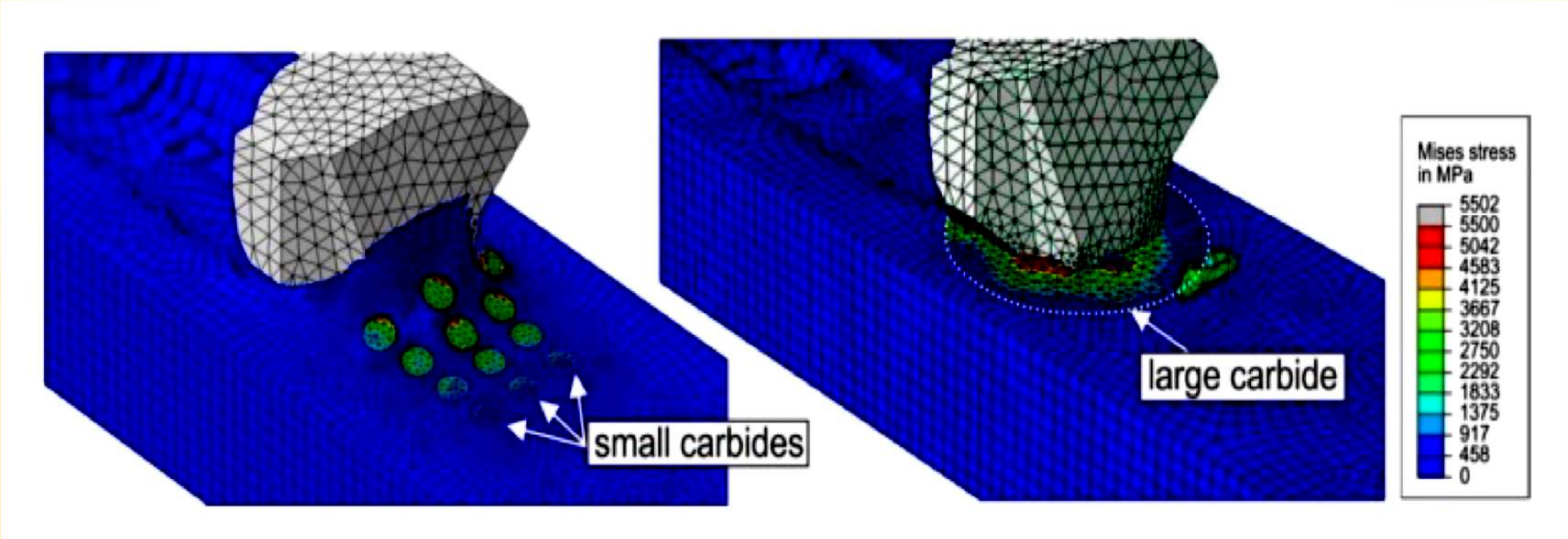

Pöhl et al. (2015)

Damage

Damage models allow predicting the damage evolution of materials at the time until the macrocrack onset, based on the resulting functions of the stress and strain fields. For metallic alloys, the damage particularly derives from nucleation and coalescence of microcracks and voids (LEMAITRE, 1984).

Damage calculations and predictions can follow two ways described by the interaction between constitutive equations and damage models:
(i-) uncoupled damage in the numerical simulation – the stress and strain fields initially calculated (based on known geometry, material constitutive equations and applied loadings) are considered inputs of the new simulation that can map the damage areas.
(ii-) coupled damage in the numerical simulation – this approach tends to better reproduce the behavior of the materials, since the damage field immediately influences the stress and strain fields (simultaneously). According to Lemaitre (1984), the main property responsible for this effect is the stiffness or the elastic modulus of the materials.

Schematic representation of the uncoupled analysis of the damage model.

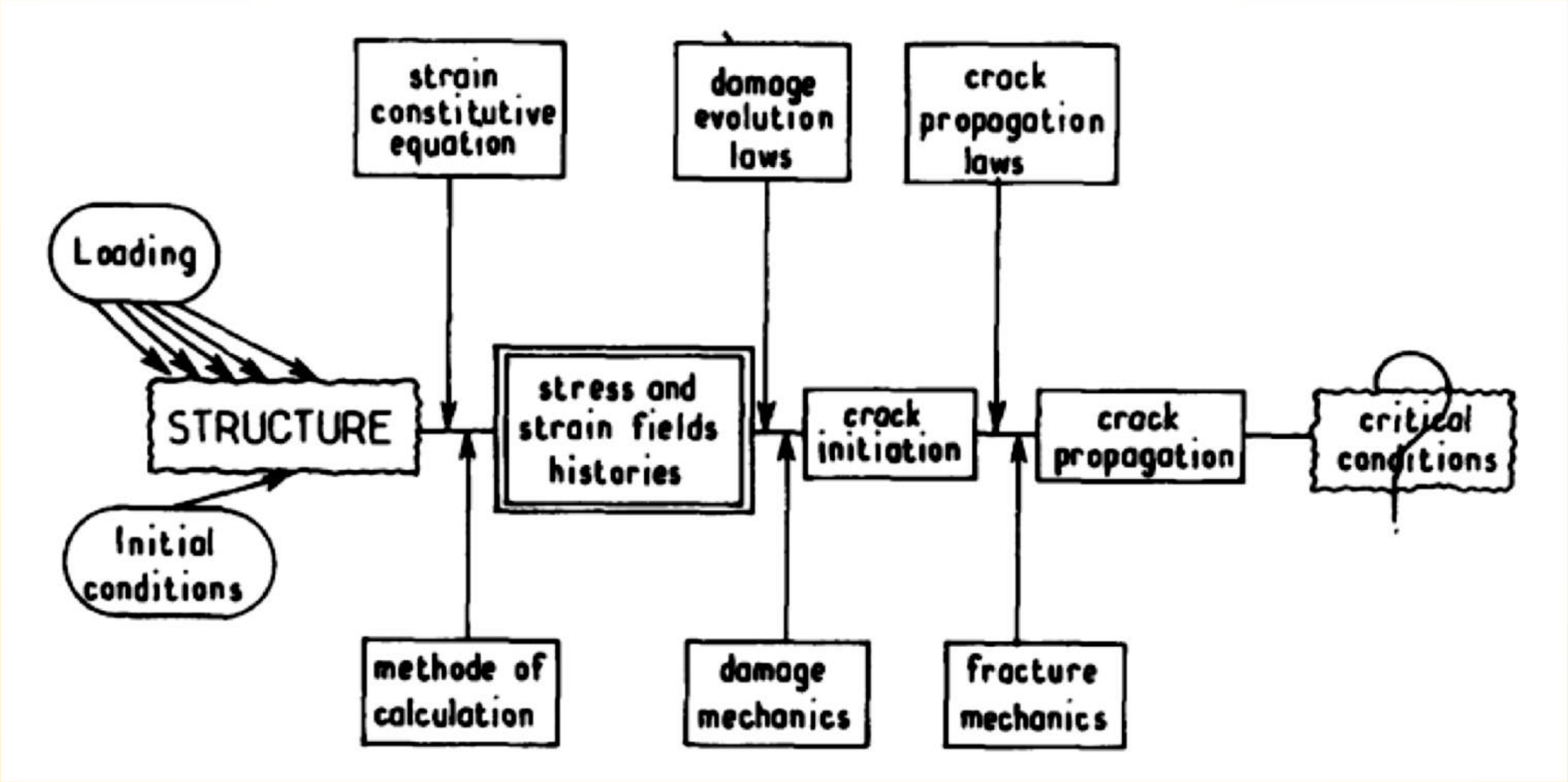

Schematic representation of the coupled analysis of the damage model.

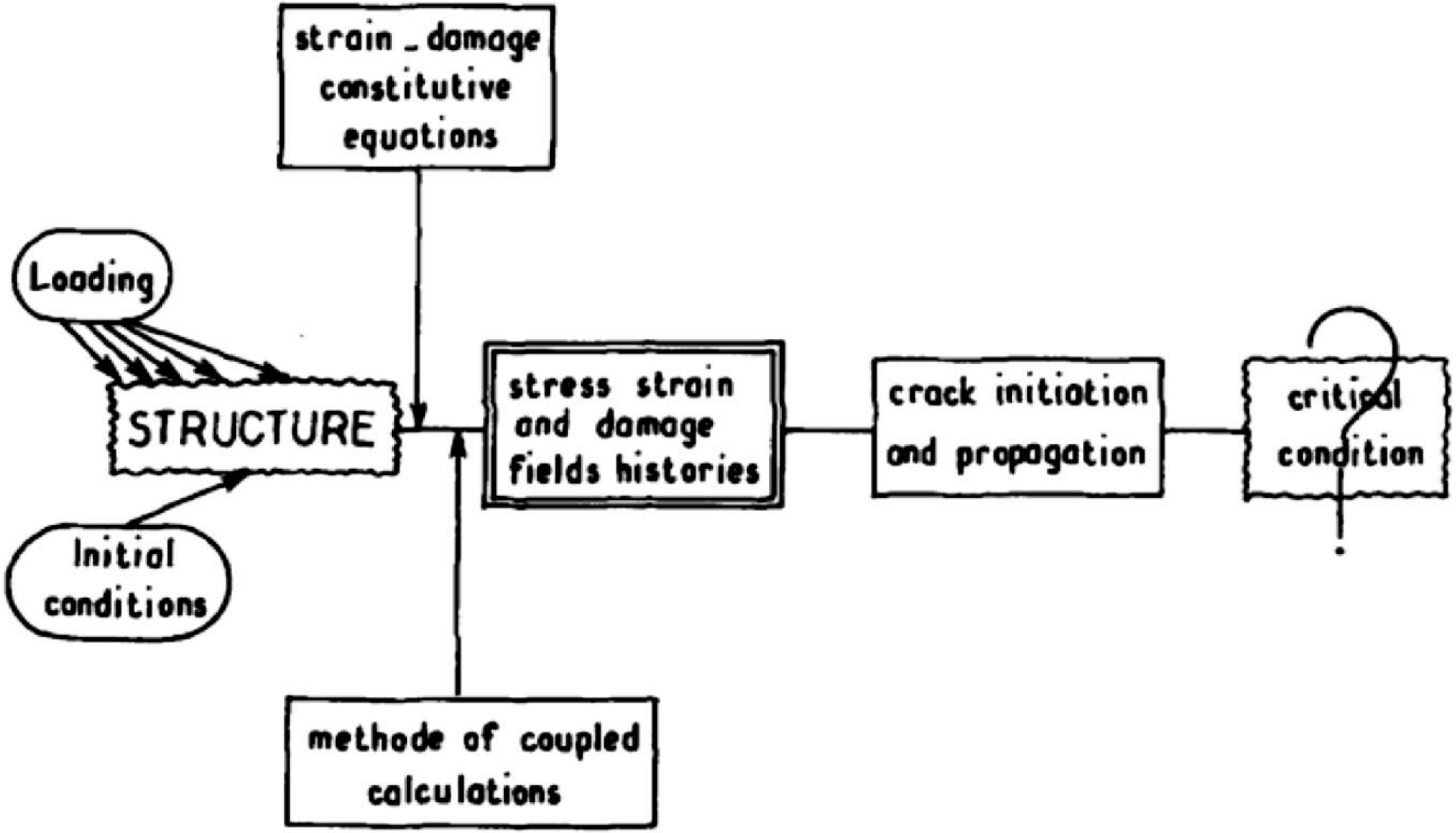

Stress-strain curve for an elastic-plastic material, in which the cumulative damage can be studied.

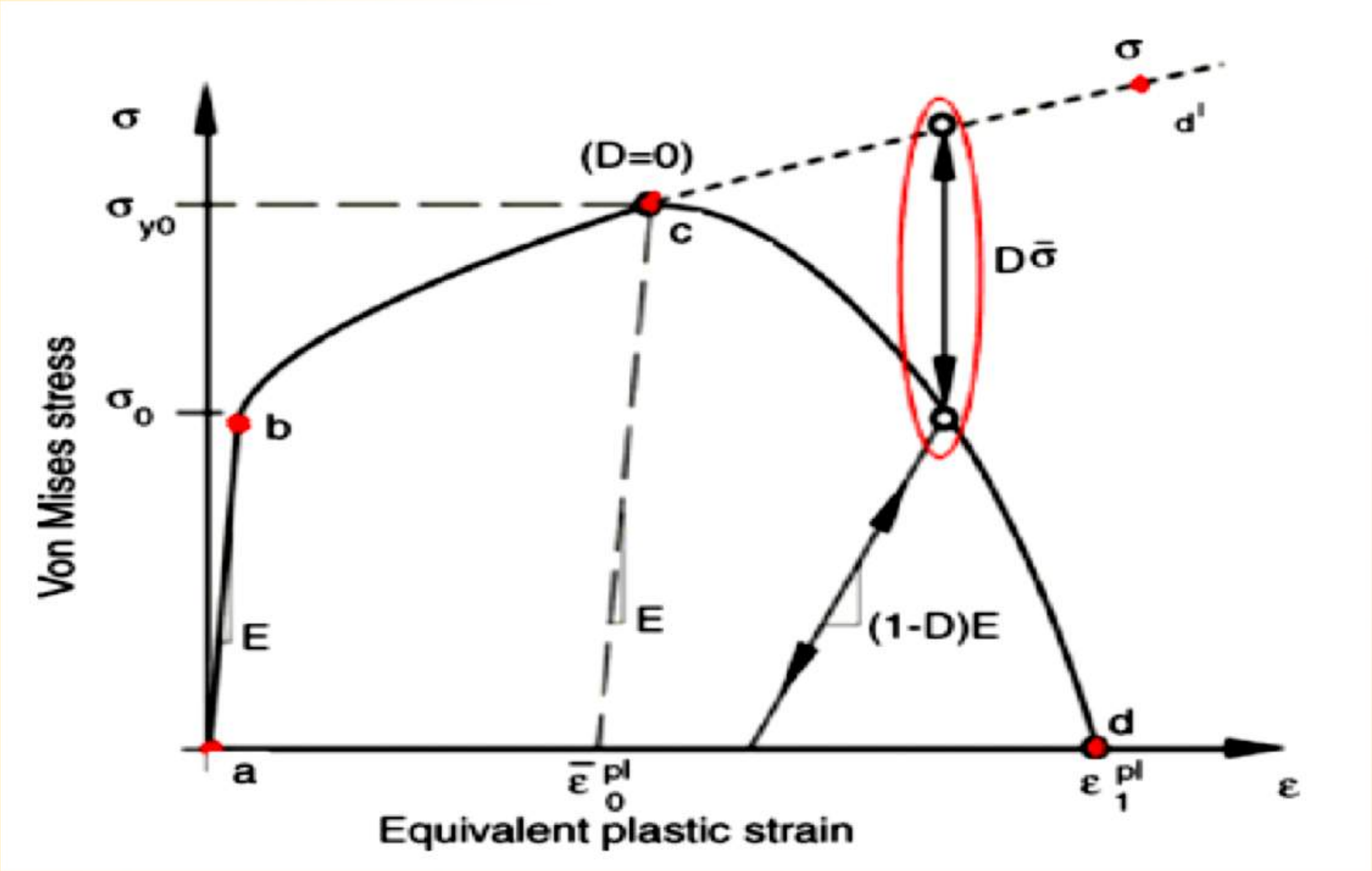

The phenomenological description of the cumulative damage for materials is given by a damage scalar parameter (D), which is dependent on the stress and strain states, strain rate and temperature.

When D is equal to 0, no damage is presented, and when D is of about 1, the material fracture occurs (LEMAITRE, 1984; LAPOVOK; SMIRNOV; SHVEYKIN, 2000).

References: (TKAYA et al., 2007; SIMULIA, 2016).

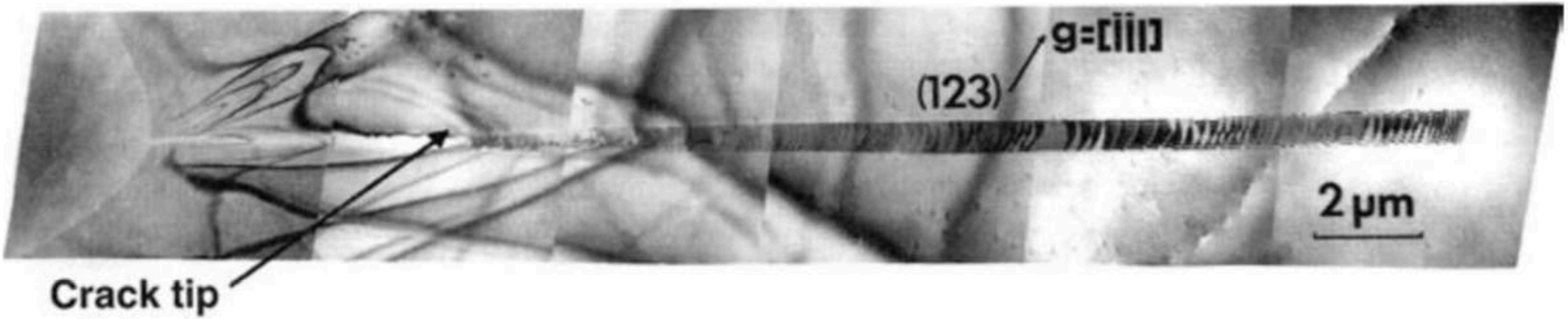

Fig. 7.9 Dislocations emitted from a crack tip in copper. (Courtesy of S. M. Ohr.)

Linear Elastic Fracture Mechanics

A nonductile material has a very low capacity to deform plastically; that is, it is not capable of relaxing peak stresses at crack-like defects.

$$\boxed{\sigma_c = \sqrt{\frac{2E\,\gamma_s}{\pi\,a}} \quad \text{(plane stress).}}$$

$$\sigma_c\sqrt{a} = \frac{1}{2}(\sigma_{\max})_c\,\sqrt{\rho} = \text{constant.}$$

$$\boxed{\sigma_c = \sqrt{\frac{2E\,\gamma_s}{\pi\,a(1-\nu^2)}} \quad \text{(plane strain).}}$$

Here, σ_c is the critical far-field or uniform stress (i.e., the stress at fracture), *a* is the crack length corresponding to σ_c, $(\sigma_{max})_c$ is the stress at the crack tip at fracture, and ρ is the root radius at the tip of the crack

Crack Propagation with Plasticity

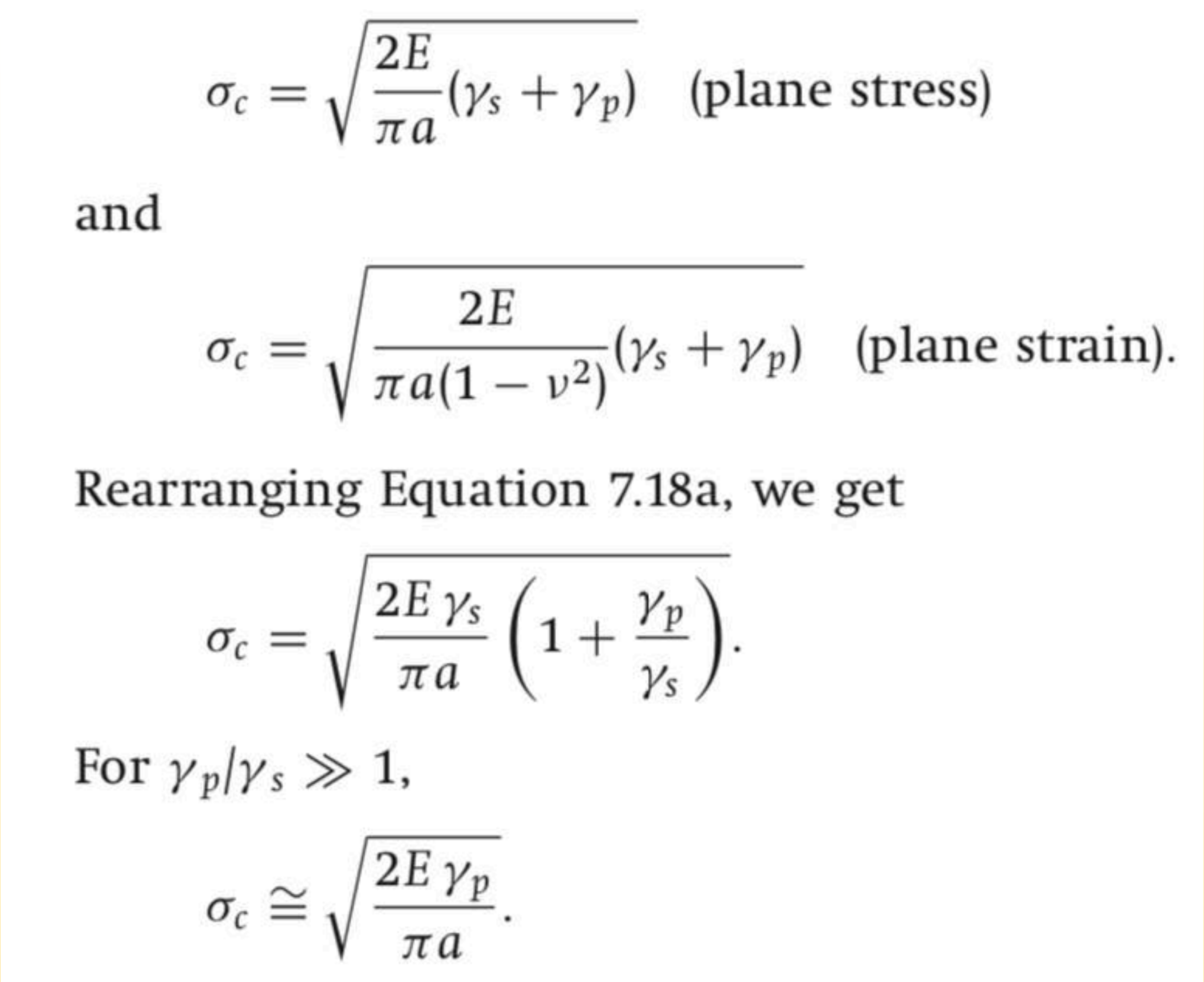

$$\sigma_c = \sqrt{\frac{2E}{\pi a}(\gamma_s + \gamma_p)} \quad \text{(plane stress)}$$

and

$$\sigma_c = \sqrt{\frac{2E}{\pi a(1-\nu^2)}(\gamma_s + \gamma_p)} \quad \text{(plane strain)}.$$

Rearranging Equation 7.18a, we get

$$\sigma_c = \sqrt{\frac{2E\,\gamma_s}{\pi a}\left(1 + \frac{\gamma_p}{\gamma_s}\right)}.$$

For $\gamma_p/\gamma_s \gg 1$,

$$\sigma_c \cong \sqrt{\frac{2E\,\gamma_p}{\pi a}}.$$

The material at the tip, however, presents resistance to crack growth. We denote this inherent material resistance by *KR* (sometimes the symbol *R* alone is used in place of *KR*.) The discipline of fracture mechanics can then be represented by a triangle as shown :

Fig. 7.10 Inherent material resistance to crack growth and its relationship to the applied stress σ and crack size a.

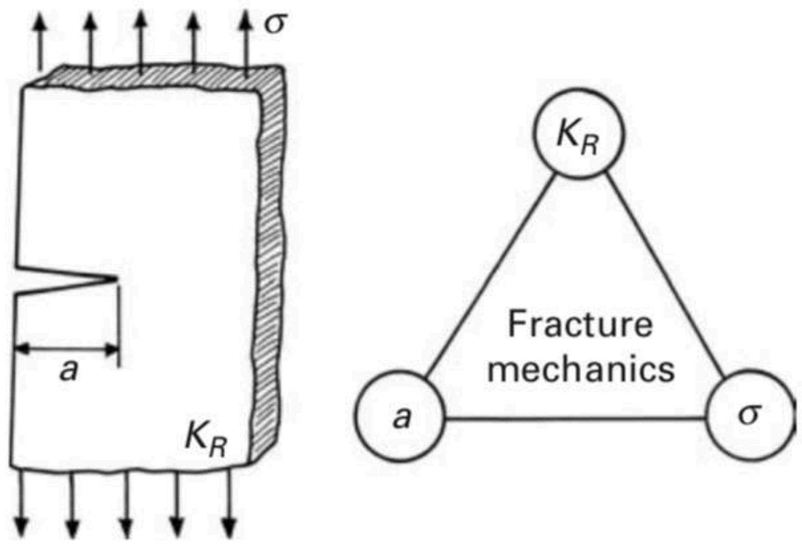

Interplay among the following three quantities:

1. The far-field stress, σ.
2. The characteristic crack length, *a*.
3. The inherent material resistance to cracking, *KR*.

$$K = \sigma\sqrt{\pi a}$$

K is the stress intensity factor for the plate and has the units (N/m^2) √m, or Pa√m, or Nm$^{-3/2}$.

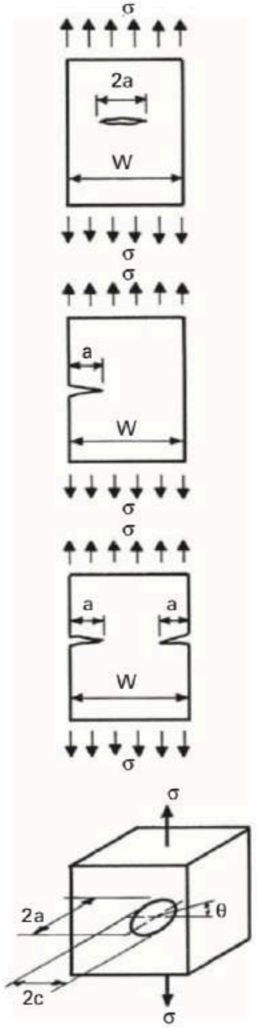

Center crack: $K_1 = Y\sigma\sqrt{\pi a}$

$$Y = 1 + 0.256\left(\frac{a}{W}\right) - 1.152\left(\frac{a}{W}\right)^2 + 12.200\left(\frac{a}{W}\right)^3$$

$$\text{or } Y = \sqrt{\sec\left(\frac{\pi a}{W}\right)}$$

$$\text{or } Y = \frac{1}{\sqrt{1-\left(\frac{2a}{W}\right)^2}}$$

Single edge notch: $K_1 = Y\sigma\sqrt{\pi a}$

$Y = 1.12$ for small cracks

$$\text{or } Y = 1.12 - 0.231\left(\frac{a}{W}\right) + 10.55\left(\frac{a}{W}\right)^2 - 21.72\left(\frac{a}{W}\right)^3 + 30.39\left(\frac{a}{W}\right)^4$$

up to $a/W = 0.6$

Double edge notch: $K_1 = Y\sigma\sqrt{\pi a}$

$Y = 1.12$ for small cracks

$$\text{or } Y = \frac{1.222 - 0.561\left(\frac{a}{W}\right) - 0.205\left(\frac{a}{W}\right)^2 + 0.471\left(\frac{a}{W}\right)^3 - 0.190\left(\frac{a}{W}\right)^4}{\sqrt{1-\frac{a}{W}}}$$

Embedded Cracks

Elliptical crack: $K_1 = Y\sigma\sqrt{\pi a}$

$$Y = \left(\sin^2\theta + \frac{a^2}{c^2}\cos^2\theta\right)^{1/4} \Big/ \left(\frac{3\pi}{8} + \frac{\pi}{8}\frac{a^2}{c^2}\right)$$

Circular crack: $K_1 = Y\sigma\sqrt{\pi a}$

$$Y = \frac{2}{\pi}$$

Fig. 7.13 Some common load and crack configurations and the corresponding expressions for the stress intensity factor, *K*.

Plastic-Zone Size Correction

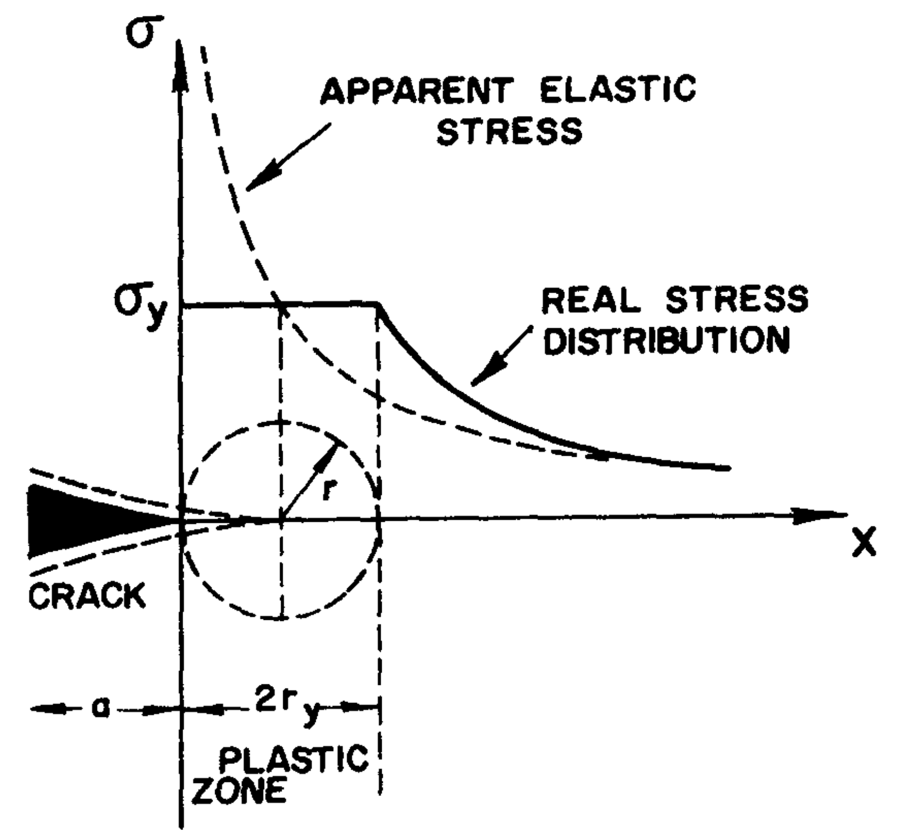

Figure 7.13 Plastic-zone correction. The effective crack length is $(a + r_y)$.

$$\sigma_y = \frac{K}{\sqrt{2\pi r_y}}$$

$$r_y = \frac{1}{2\pi}\left(\frac{K}{\sigma_y}\right)^2$$

$$r_y \approx \frac{1}{2\pi}\left(\frac{K}{\sigma_y}\right)^2$$

$$r_y \approx \frac{1}{6\pi}\left(\frac{K}{\sigma_y}\right)^2$$

$$(2a)_{eff} = 2(a + r_y)$$

Izabel Machado – machadoi@usp.br

Plastic-Zone Size Correction

Dugdale - BCS

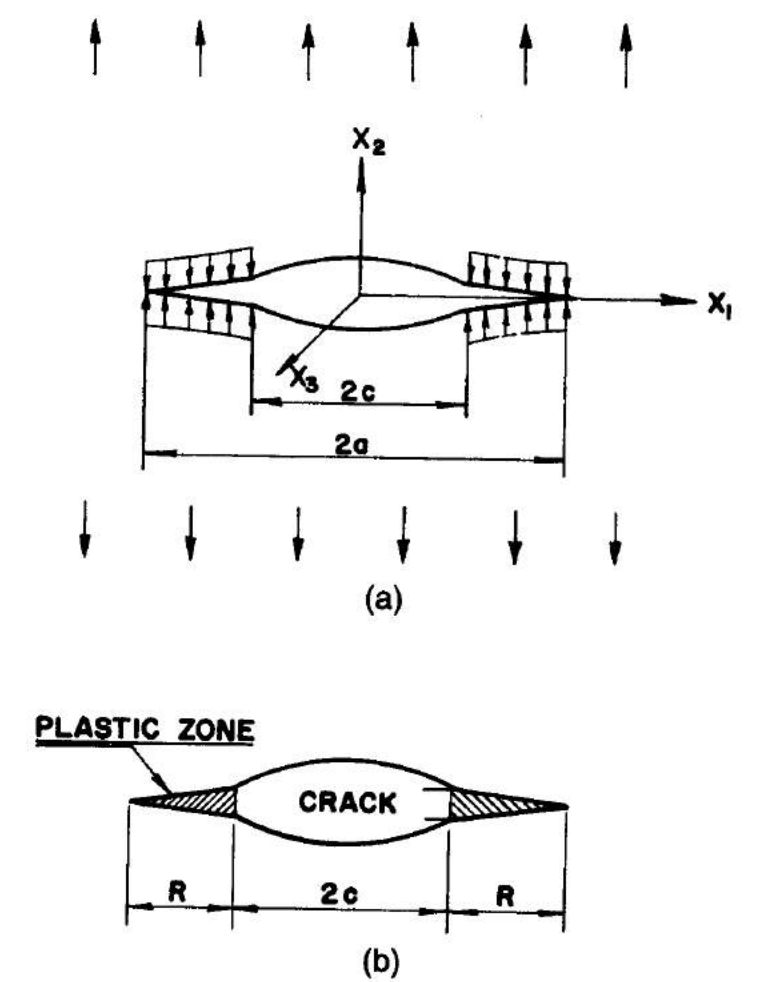

Figure 7.14 Dugdale–Bilby–Cottrell–Swinden model of a crack.

$$\frac{c}{a} = \cos\frac{\pi\sigma}{2\sigma_y}$$

Quando $\sigma \ll \sigma_y$

$$\frac{R}{c} \approx \frac{\pi^2}{8}\left(\frac{\sigma}{\sigma_y}\right)^2$$

ou

$$R \approx \frac{\pi}{8}\left(\frac{K}{\sigma_y}\right)^2$$

Izabel Machado – machadoi@usp.br

Plastic-Zone Size Correction

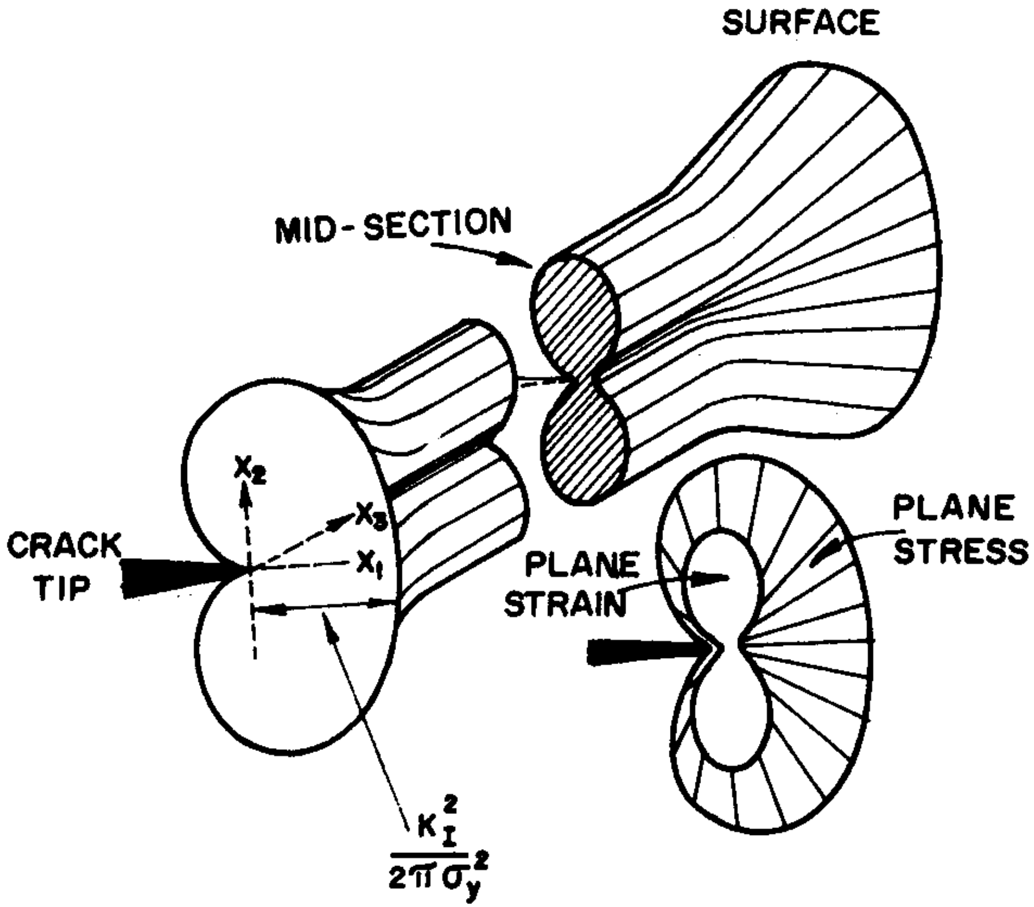

Figure 7.15 Formal representation of the plastic zone at the crack tip in a through-the-thickness crack in a plate.

Izabel Machado – machadoi@usp.br

Plastic-Zone Size Correction

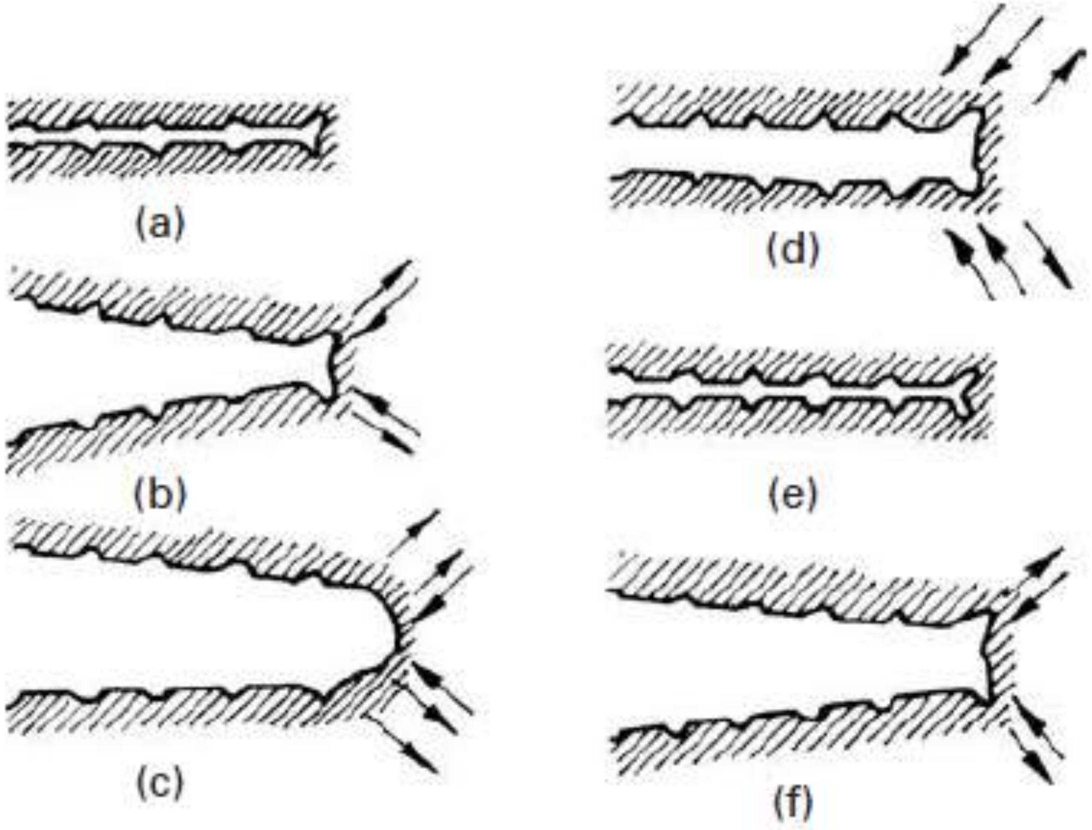

Fig. 14.18 Fatigue crack growth by a plastic blunting mechanism. (a) Zero load. (b) Small tensile load. (c) Maximum tensile load. (d) Small compressive load. (e) Maximum compressive load. (f) Small tensile load. The loading axis is vertical (After C. Laird, in *Fatigue Crack Propagation*, ASTM STP 415 (Philadelphia: ASTM, 1967), p. 131.)

Variação da tenacidade à fratura com a espessura

Estado plano de tensão ou de deformação

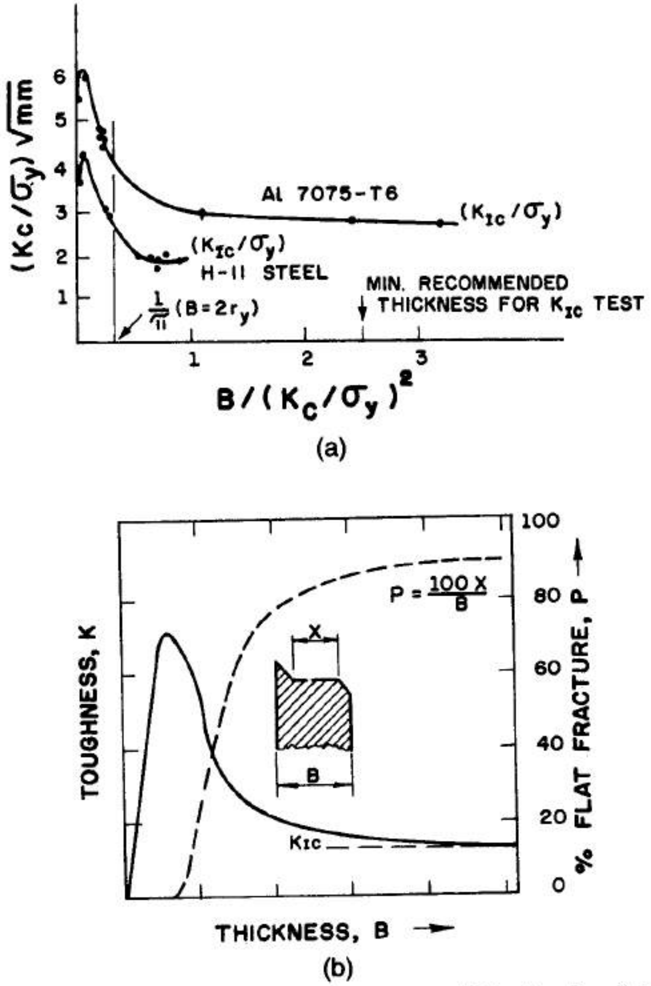

Figure 7.16 (a) Variation in fracture toughness (K_c) with plate thickness (B) for Al 7075-T6 and H-11 Steel. (Reprinted with permission from J. E. Srawley and W. F. Brown, ASTM STP 381, ASTM, Philadelphia, pp. 133, and G. R. Irwin, in *Encyclopaedia of Physics*, Vol. VI (Heidelberg: Springer Verlag, 1958); see also *J. Basic Eng., Trans. ASME, 82* (1960) 417. (b) Schematic variation of fracture toughness K_c and percentage of flat fracture P with the plate thickness B.

O estado de tensões elástico é influenciado pela espessura da placa. O material se deforma e o volume é mantido constante. Grandes deformações em x1 e em x2 levam à uma diminuição na deformação x3 (paralela à frente de propagação da trinca). A relação entre a zona plástica e a espessura da placa é dada por:

$$\frac{B}{2r_y} = \pi \frac{B}{(Kc/\sigma_y)^2}$$

Parâmetros de tenacidade à fratura

Força para extensão da trinca G (Irwin)

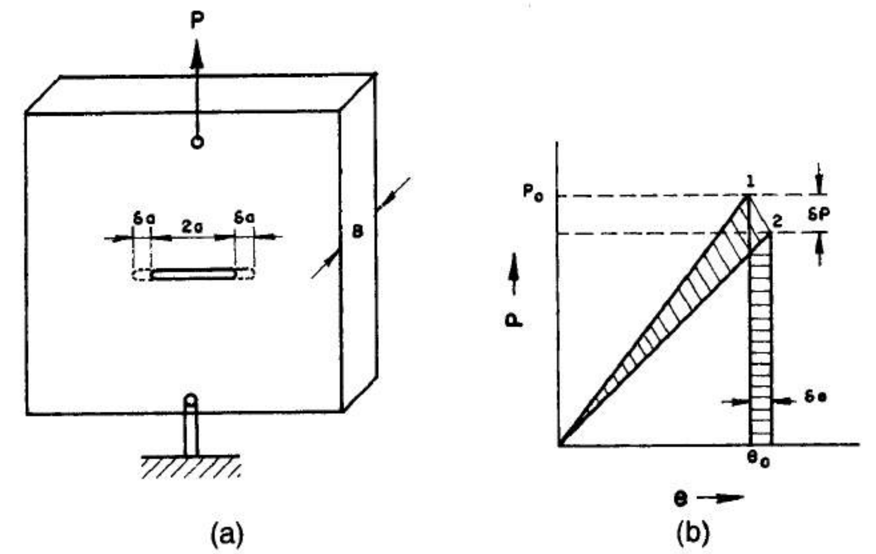

Figure 7.17 (a) Elastic body containing a crack of length 2*a* under load *P*. (b) Diagram of load *P* versus displacement *e*.

Antes da propagação da trinca a energia potencial armazenada é dada por:

Após a propagação da trinca a energia potencial armazenada é dada por:

onde

Parâmetros de tenacidade à fratura

Força para extensão da trinca G

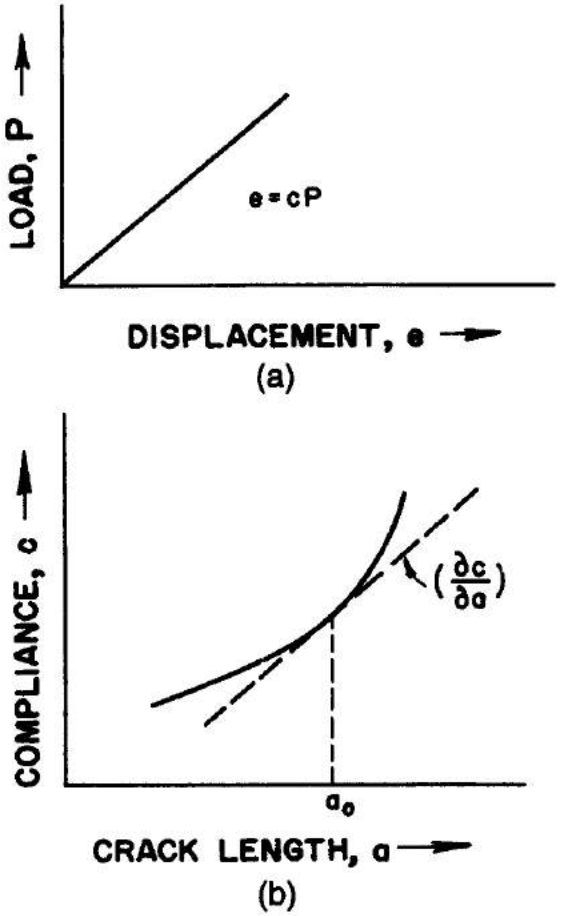

Figure 7.18 (a) Load *P* versus displacement *e*. Compliance *c* is the inverse of the slope of this curve. (b) Compliance *c* versus crack length *a*. a_0 is the initial crack length.

$$G = \frac{P^2 \delta c}{2B\,\delta a}$$

Parâmetros de tenacidade à fratura

COD – Crack opening displacement

A ocorrência de deformação plástica na ponta da trinca resulta em uma deslocamento das duas partes da trinca sem que haja propagação da mesma. Esse deslocamanto é chamado de “crack opening displacement”. δc seria o valor crítico dessa “abertura”.

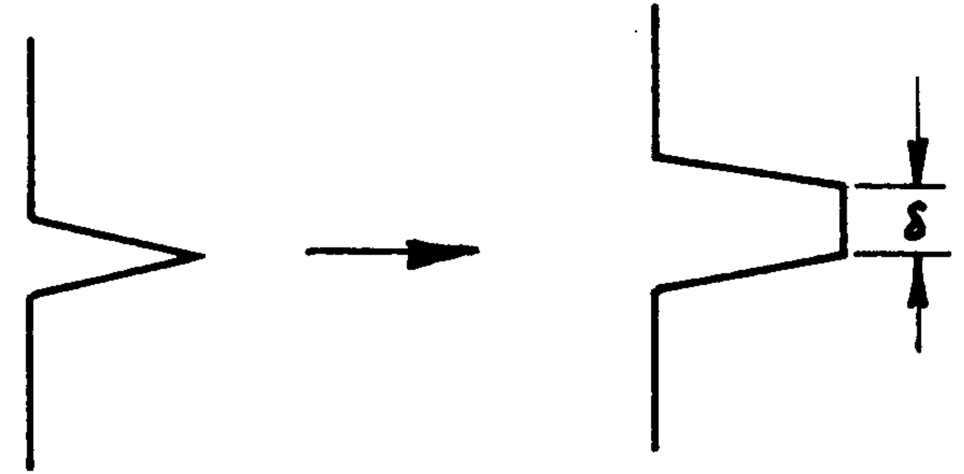

Figure 7.19 Crack opening displacement.

Parâmetros de tenacidade à fratura

COD – Crack opening displacement

Tomando a dedução de Irwin para a zona plástica, o CTOD seria o deslocamento das faces da trinca ($\theta=180^{o}$) para uma distância r=ry da ponta da trinca de comprimento a.

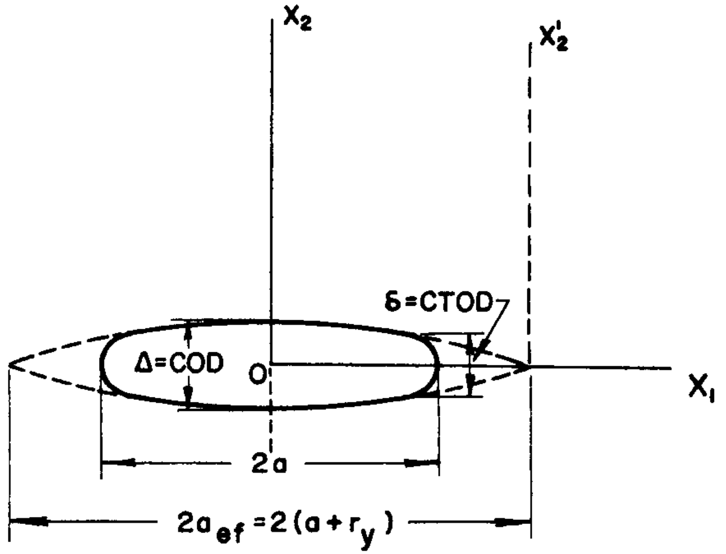

Figure 7.20 Relationship between crack opening displacement (COD, Δ), crack-tip opening displacement (CTOD, δ), crack length ($2a$), and size of plastic zone (r_y).

Parâmetros de tenacidade à fratura

Integral J

A integral J dá o valor da energia necessária à propagação de uma trinca em uma material elasto-plástico.

Em uma sistema fechado (contorno Γ), um corpo submetido à esforços externos terá tensão internas relativas à esses esforços. Pela teoria da conservação de energia a integral J será zero para este sistema fechado.

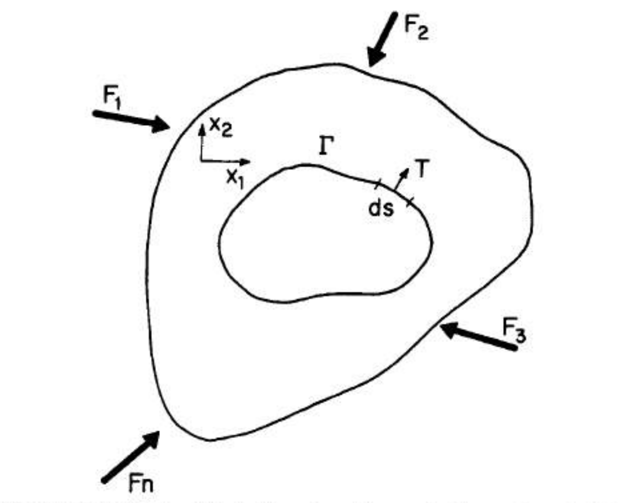

Figure 7.21 A body subjected to external forces $F_1, F_2, \ldots, F_n$ and with a closed contour Γ.

$$J = \int_{\Gamma} \left(W dx_2 - T \frac{\partial u}{\partial x_1} ds \right) = 0$$

$$W = \int_{0}^{\Sigma_{ij}} \sigma_{ij} d\varepsilon_{ij}$$

Parâmetros de tenacidade à fratura

Integral J

A energia ao longo de dois caminhos diferentes tem o mesmo valor. A integral J ao longo da trinca é independente do caminho. A integral J entorno da trinca é igual a mudança de energia potencial para a propagação da trinca da. Para um corpo de espessura B tem-se:

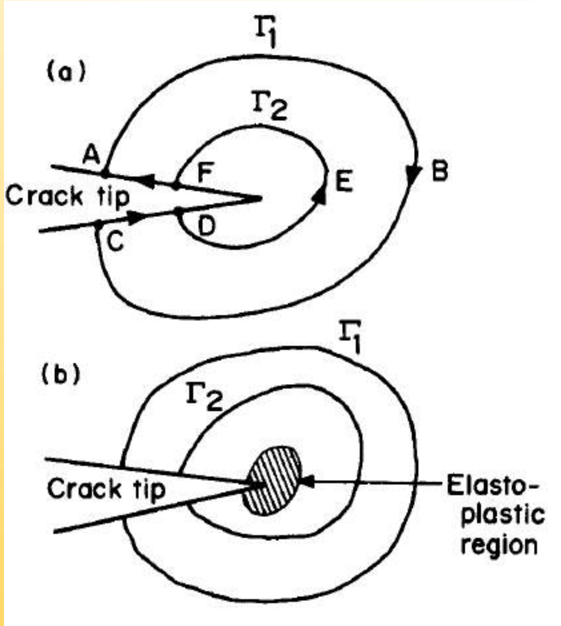

Figure 7.22 Eshelby contours around cracks.

$$J = -\frac{1}{B}\frac{\delta U}{\delta a}$$

Parâmetros de tenacidade à fratura

Integral J

A integral J é limitada ao início de propagação da trinca seja de forma estável ou instável.

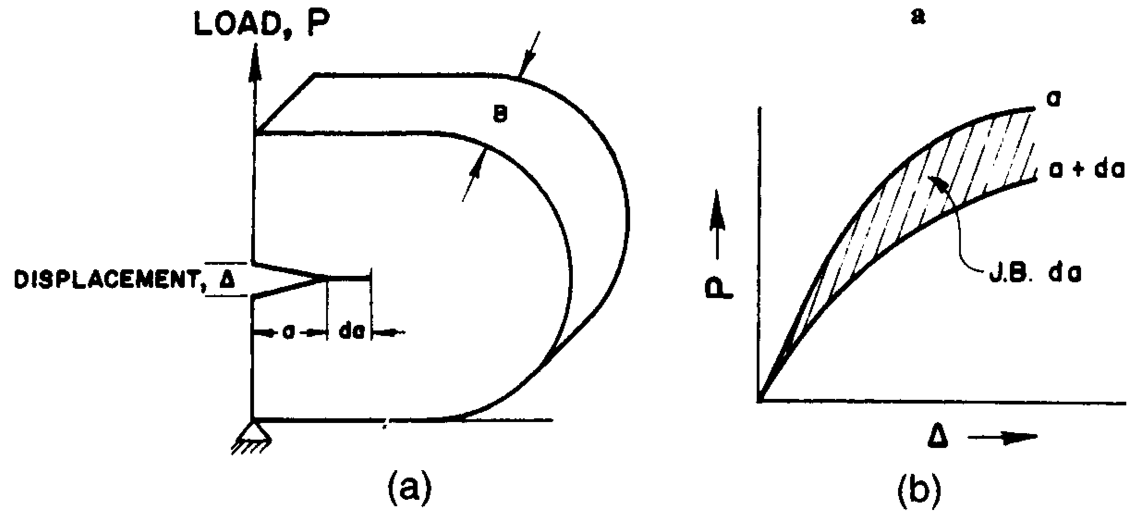

Figure 7.23 Physical interpretation of the *J* integral. The *J* integral represents the difference in potential energy (shaded area) of identical bodies containing cracks of length *a* and *a* + *da*.

Izabel Machado – machadoi@usp.br

Parâmetros de tenacidade à fratura

Curva R

A curva R caracteriza a resistência do material à fratura durante a propagação da trinca de forma lenta e estável.

Com o aumento da carga a força para a propagação da trinca G na ponta da trinca aumenta e a resistência a à propagação da mesma R aumenta. A fratura ocorrerá quando:

$$\frac{\delta G}{\delta a} = \frac{\delta R}{\delta a}$$

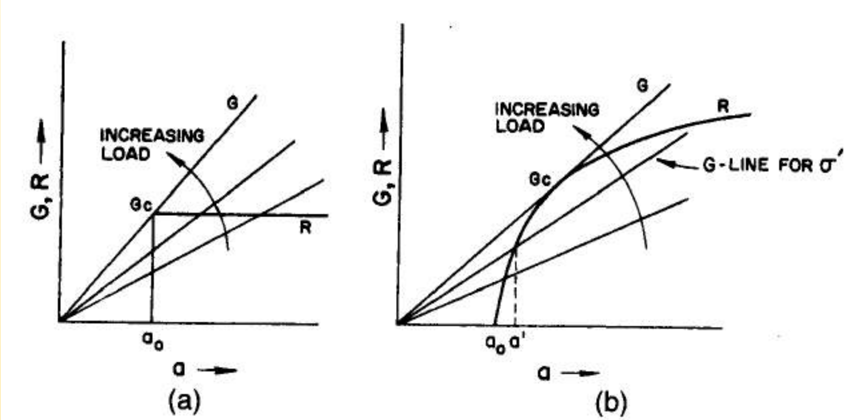

Figure 7.24 *R* curves for (a) brittle material and (b) ductile material.

Parâmetros de tenacidade à fratura

K (fator de intensificação de de tensão),

G (força para propagação da trinca),

J (balanço energético) ,

δ (COD e CTOD crack opening displacement),

R

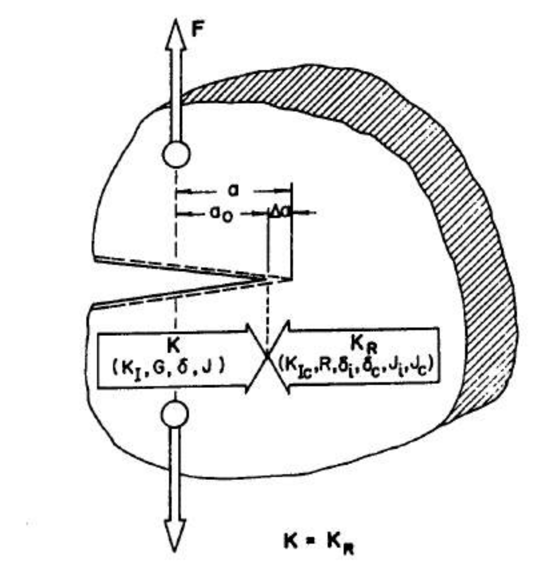

Figure 7.25 Different parameters describing the growth of a crack.

Estado plano de deformação

$$J = G = {K^2(1-\upsilon^2)}\Big/{E} = \lambda \sigma_y \delta$$

Izabel Machado – machadoi@usp.br

STATISTICAL ANALYSIS OF FAILURE STRENGTH

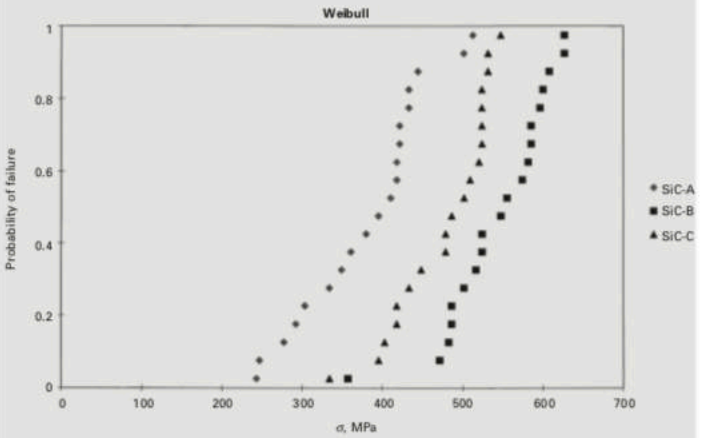

Fig. E7.8.3

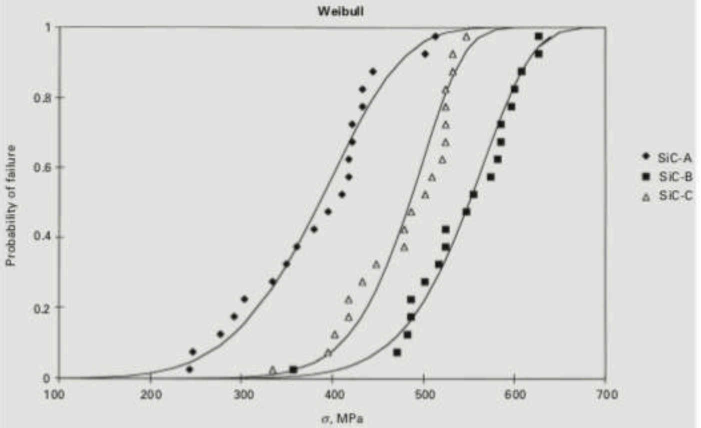

Fig. E7.8.4

Table E7.8.2

Specimen	m	σ_0 (MPa)	Average Stress ± S.D. (MPa)
SiC-A	5.61	411.3	380.7 ± 63.1
SiC-B	9.10	572.1	542.0 ± 52.6
SiC-N	9.22	502.9	476.8 ± 48.7

S.D. = Standard deviation.

Hard and superhard materials: A computational perspective

Hard and superhard materials are essential for a myriad of scientific, biomedical, and industrial applications. Their ability to resist indentation stems from the relationship between the crystal structure, chemical composition, and microstructure.

Indentation measurements progress through two stages; the first response measured upon indentation is elastic deformation (reversible) followed by plastic (irreversible) deformation. The Young's (E) mod- ulus can be extracted from the elastic behavior of a material during the reversible stage.

There are three different categories of indentation: macroindentation, microindentation, and nanoindentation.

http://dx.doi.org/10.1016/j.jssc.2018.10.048

Hardness

Analyzing the different types of indentation techniques highlights the fact that each approach measures a range of length scales and probes distinct deformation mechanisms making the hardness values incomparable.

Tables to convert the values obtained using different hardness method measurements exist; however, the conversion is not always reliable because the stress-states based on each indenter causes various deformation modes making any comparison qualitative at best.

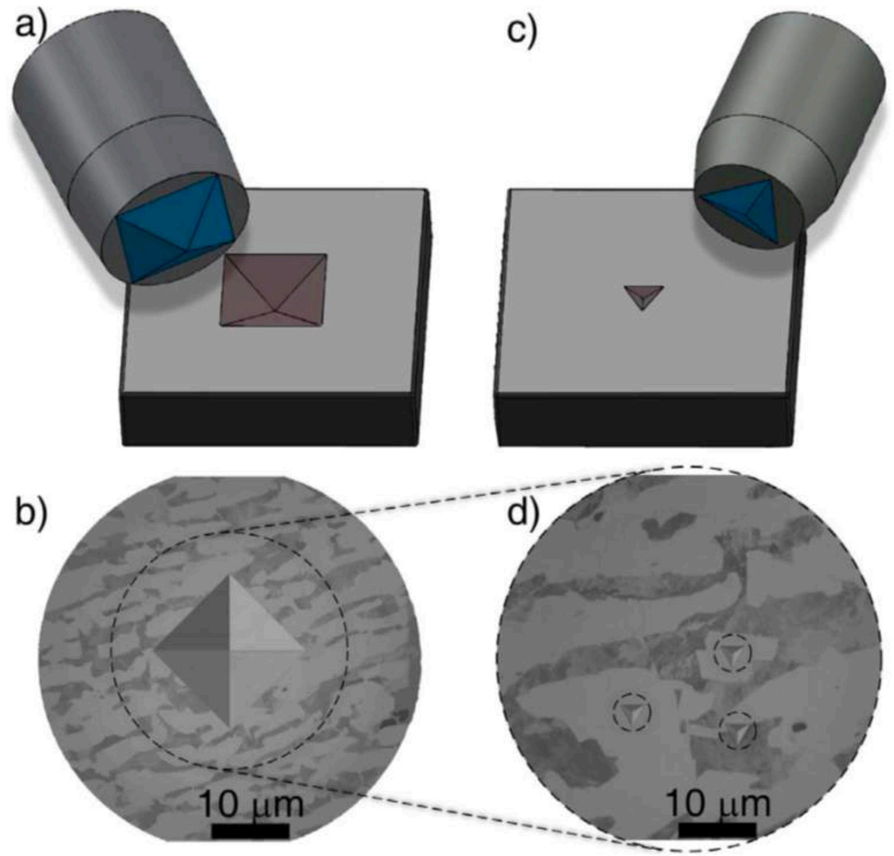

Fig. 1. a) Schematic of Vickers microindentation tip. b) The imprint of Vickers microindentation yields the average mechanical properties by probing across multiple grains, grain boundaries, and potential impurities in a single sample. c) Schematic of Berkovich nanoindentation tip. d) The imprint of the Berkovich nanoindenter tip shows how the indentations can measure the hardness locally on specific grains, or across grain boundaries.

http://dx.doi.org/10.1016/j.jssc.2018.10.048

Hardness

One of the most significant challenges in using computation to develop a material with outstanding resistance to deformation is the fact that **hardness is clearly not a fundamental property**.

Hardness, in fact, represents a collective response of atoms on an arbitrary scale that depends on the measurement technique.

The material's microstructure, grain size, grain boundaries, secondary phase hardening, inhomogeneities in composition, dispersion of the impurities, and structural defects significantly influence the hardness and must be considered.

The fact that hardness measurements are also sensitive to the deformation history of a specimen, meaning residual stresses are shown to dramatically influ- ence these measurements, especially in metals

Modeling indentation and hardness through molecular dynamics

The advancement of computational codes and resources now allows highly-parallel molecular dynamic simulations.

MD simulations have been essential in establishing the relationship between mechanical properties and the microstructure.

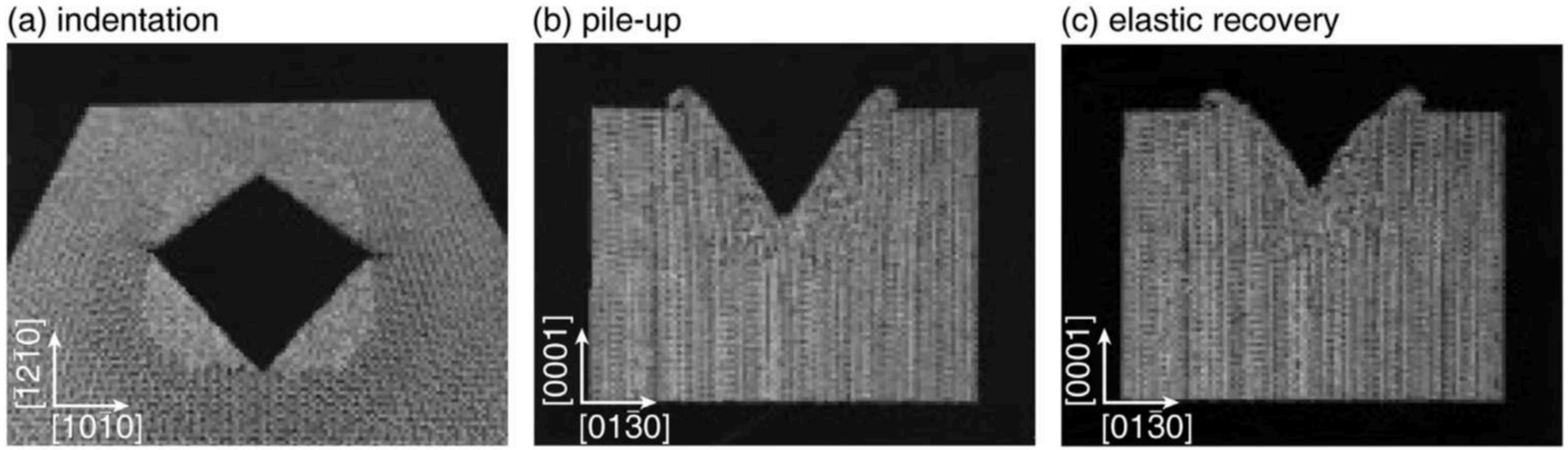
(a) indentation
(b) pile-up
(c) elastic recovery

Fig. 2. a) Indentation of α-Si_3N_4 modeled using molecular dynamics showing cracks and (b) pile-up for fully loaded configuration. (c) Unloaded configuration shows some elastic recovery. The MD simulation considered 10,614,240 atoms.
Modified from [30].

http://dx.doi.org/10.1016/j.jssc.2018.10.048

Mechanical properties

Hard and superhard materials: A computational perspective

Empirical and semi-empirical approximations of intrinsic hardness

An approximation for hardness stemming from a more atomic definition of the bond strength was also derived based on Eq.

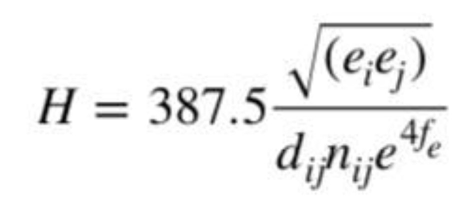

$$H = 387.5\frac{\sqrt{(e_i e_j)}}{d_{ij} n_{ij} e^{4f_e}}$$

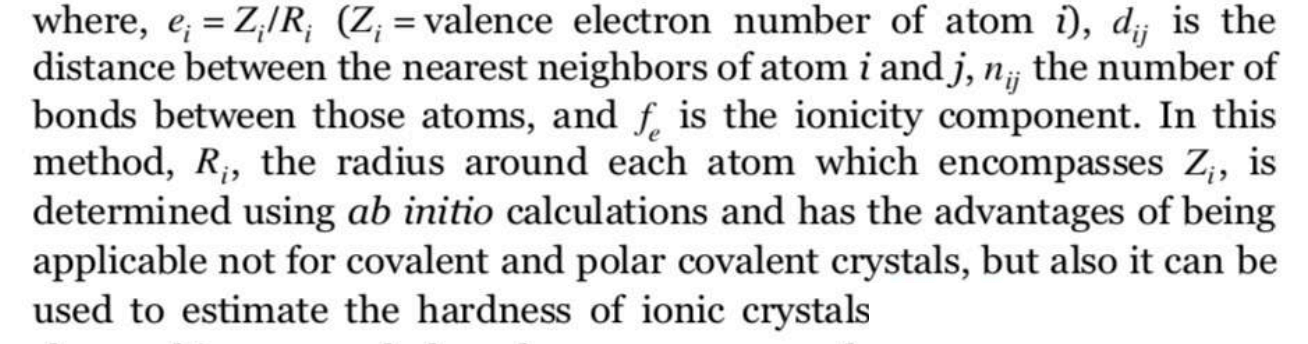

where, $e_i = Z_i/R_i$ (Z_i = valence electron number of atom i), d_{ij} is the distance between the nearest neighbors of atom i and j, n_{ij} the number of bonds between those atoms, and f_e is the ionicity component. In this method, R_i, the radius around each atom which encompasses Z_i, is determined using *ab initio* calculations and has the advantages of being applicable not for covalent and polar covalent crystals, but also it can be used to estimate the hardness of ionic crystals

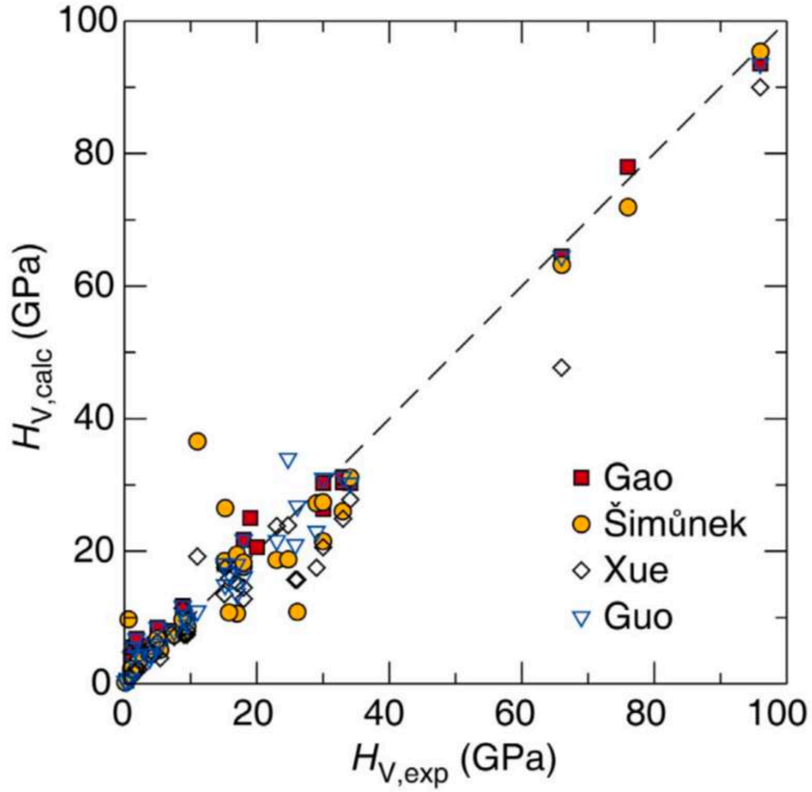

Fig. 3. Comparison between calculated (intrinsic) hardness ($H_{V,calc}$) using multiple semi-empirical models and the experimentally measured Vickers hardness ($H_{V,exp}$) demonstrate reasonable agreement within the scope of studied compounds. The figure is taken from [49] with permission.

http://dx.doi.org/10.1016/j.jssc.2018.10.048

Bulk (B) and shear modulus (G)

$$H_{V,calc} = 0.0963B$$

$$H_{V,calc} = 0.1769G - 2.899$$

$$H_{V,calc} = 0.1475G$$

$$H_{V,calc} = 0.0608E$$

$$H_{V,calc} = (1 - \nu)E/[6(1 + \nu)]$$

$$H_{V,calc} = 2(G^3/B^2)^{0.585} - 3$$

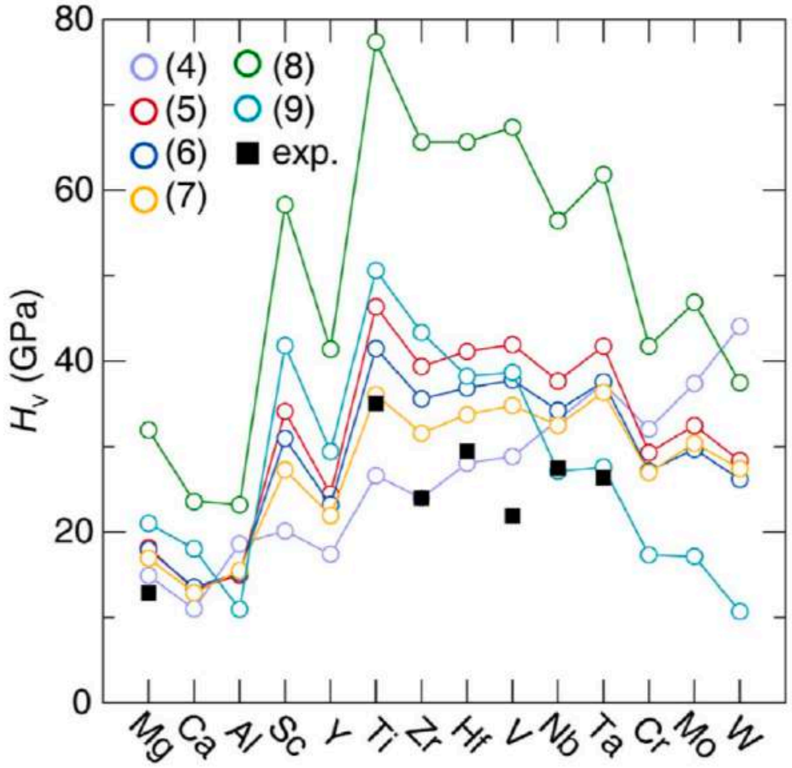

Fig. 5. Comparison of microscopic hardness models to experimental Vickers hardness calculated using Eqs. (4)–(9) with the associated experimentally measured H_V provided as black squares where available. The figure is modified from [65].

Bulk modulus still plays a significant role in the exploration of superhard materials because it is also clear from Fig. 4 that all of the known superhard materials are ultraincompressible, whereas there are no examples of a compound with low B being superhard.

http://dx.doi.org/10.1016/j.jssc.2018.10.048

Discrete Fourier transform - With the formulation of DFT-based methods to estimate intrinsic hardness, these models have been combined with efficient, evolutionary-based structure searching methods capable of identifying entirely

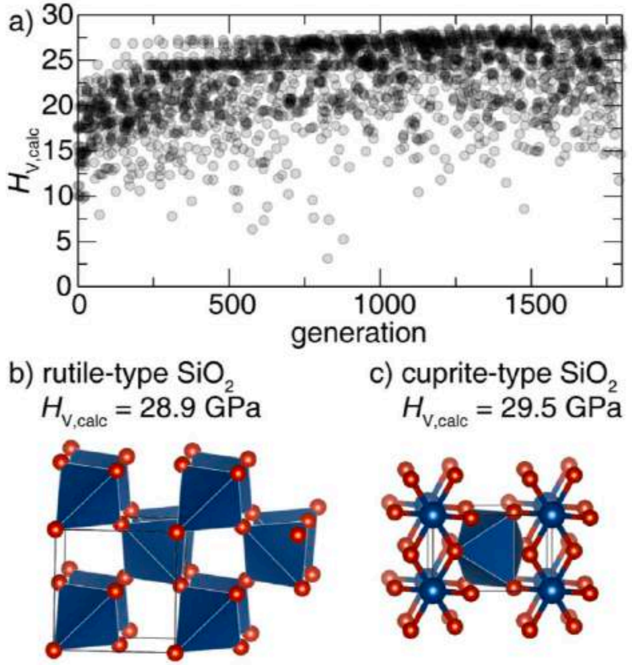

Fig. 6. (a) Evolutionary global optimization run of SiO_2 using the calculated Vickers hardness ($H_{V,calc}$) to direct the search. The darker regions on the plot occur where there are overlapping data. Two SiO_2 polymorphs are identified through the algorithm, (b) a known rutile-type and (c) a novel cuprite-type crystal structure. The figure is modified from [72].

http://dx.doi.org/10.1016/j.jssc.2018.10.048

Izabel Machado – machadoi@usp.br

Informatic-based approaches to predict mechanical properties

Unfortunately, conventional mathematical models to understand the behavior are typically unsatisfactory due to the complexity of the nature of flow behavior of metal alloys during hot deformation at high temperature and strain rates. Research has attempted to solve this problem using a feedforward backpropagation artificial neural network (ANN) to model the flow stress of 42CrMo steels

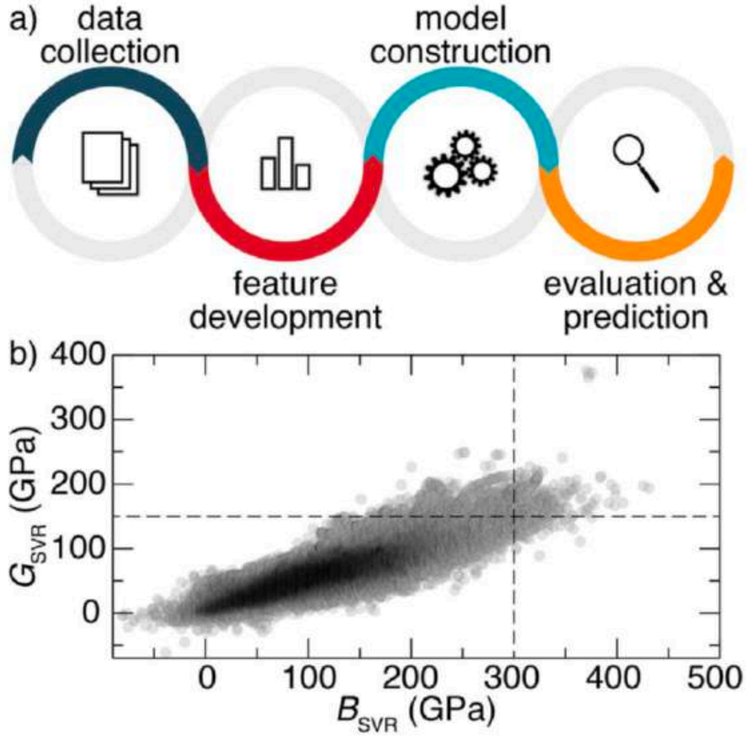

Fig. 7. a) Schematic of a typical machine learning process flow. b) Plotting the machine learning predicted shear (G_{SVR}) and bulk (B_{SVR}) moduli of 118,288 inorganic compounds suggests that compounds falling in the right top corner are potentially hard or superhard. The darker regions on the plot occur where there are overlapping data. The figure is modified from [95].

http://dx.doi.org/10.1016/j.jssc.2018.10.048

Investigating the role of defects on hardness from first principles

Structural defects significantly influence the mechanical properties of solid-state, inorganic materials. Structural defects are categorized as point defects such as vacancies and interstitials, line defects including dislocations and grain boundaries, and volumetric defects like voids and pores. Dislocation and grain boundaries, in particular, are a fundamental component of most deformation mechanisms and have been studied for decades

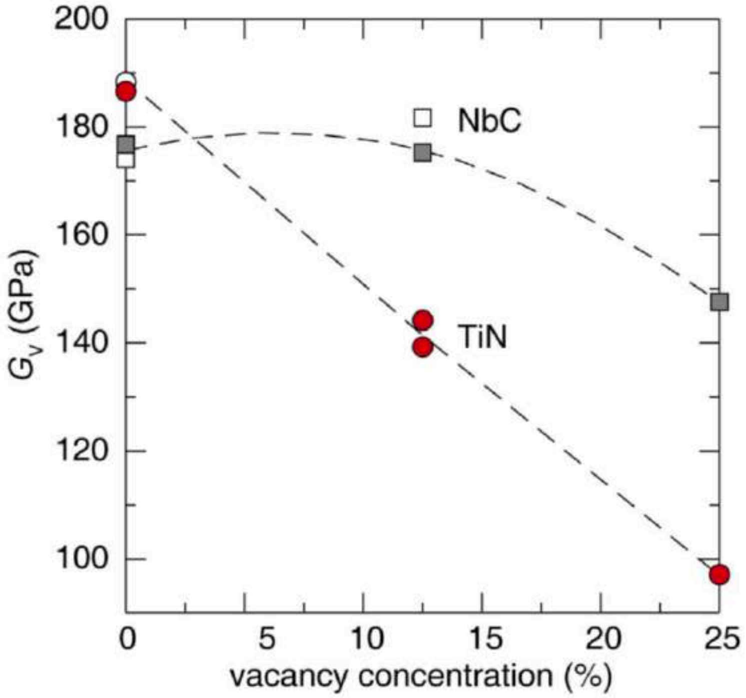

Fig. 8. Calculated Voigt elastic stiffness (G_V) at different vacancy concentrations in NbC$_x$ (squares) and TiN$_x$ (circles). Experimental data are also plotted as the open circles for TiN$_x$ and open boxes for NbC$_x$ for comparison. Dashed lines are guides for the eye. The figure is modified from [113].

http://dx.doi.org/10.1016/j.jssc.2018.10.048

Investigating the role of defects on hardness from first principles

Vacancies can influence the intrinsic hardness of materials in different ways. It is experimentally observed that hardness and elastic moduli of transition metal nitrides (TiN_x, ZrN_x, and HfN_x) deteriorates as vacancy concentration increases; however, the hardness of transition metal carbides such as NbC_x and TaC x increases as the function of vacancy concentration.

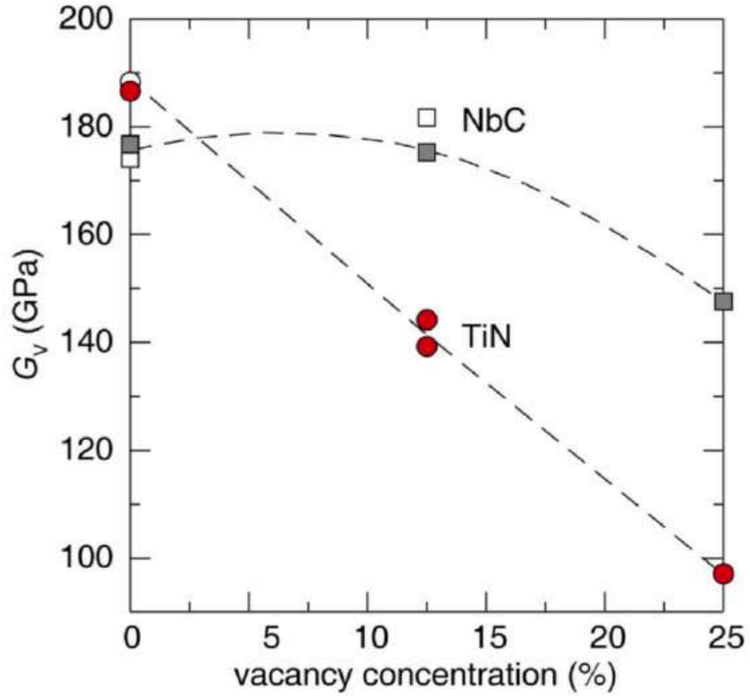

Fig. 8. Calculated Voigt elastic stiffness (G_V) at different vacancy concentrations in NbC_x (squares) and TiN_x (circles). Experimental data are also plotted as the open circles for TiN_x and open boxes for NbC_x for comparison. Dashed lines are guides for the eye. The figure is modified from [113].

http://dx.doi.org/10.1016/j.jssc.2018.10.048

Mechanical properties

Hard and superhard materials: A computational perspective

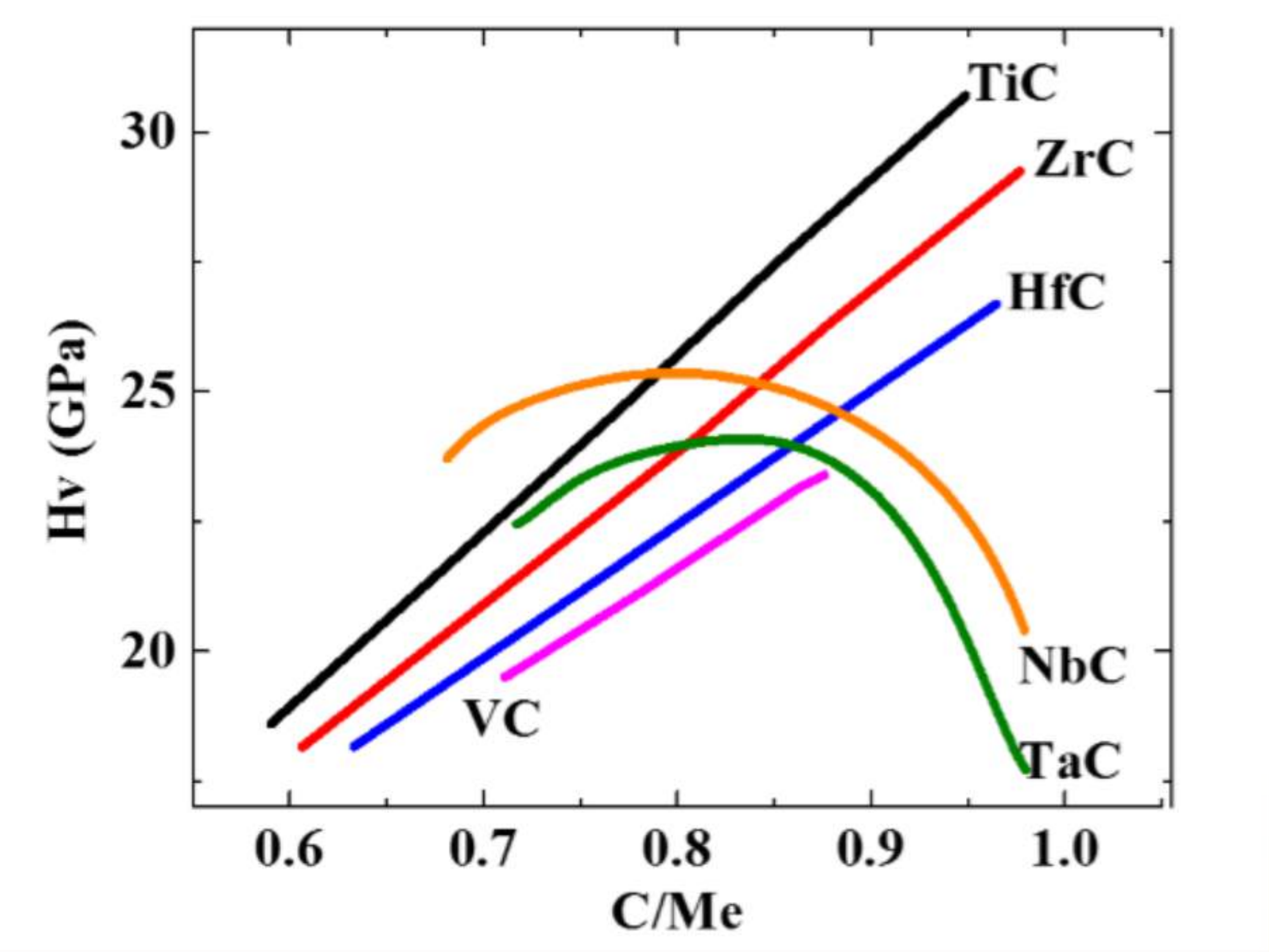

Taken from - Vinitskii I. “Relation between the properties of monocarbides of groups IV–V transition metals and their carbon content.” Powder Metall Met Ceram1972;11:488–93.

http://dx.doi.org/10.1016/j.jssc.2018.10.048

Evaluation of abrasive mechanisms in metallic alloys during scratch tests: a numerical-experimental study in micro-scale

Vanessa Seriacopi Thesis

Hard and superhard materials: A computational perspective
Aria Mansouri Tehrani, Jakoah Brgoch
http://dx.doi.org/10.1016/j.jssc.2018.10.048
*

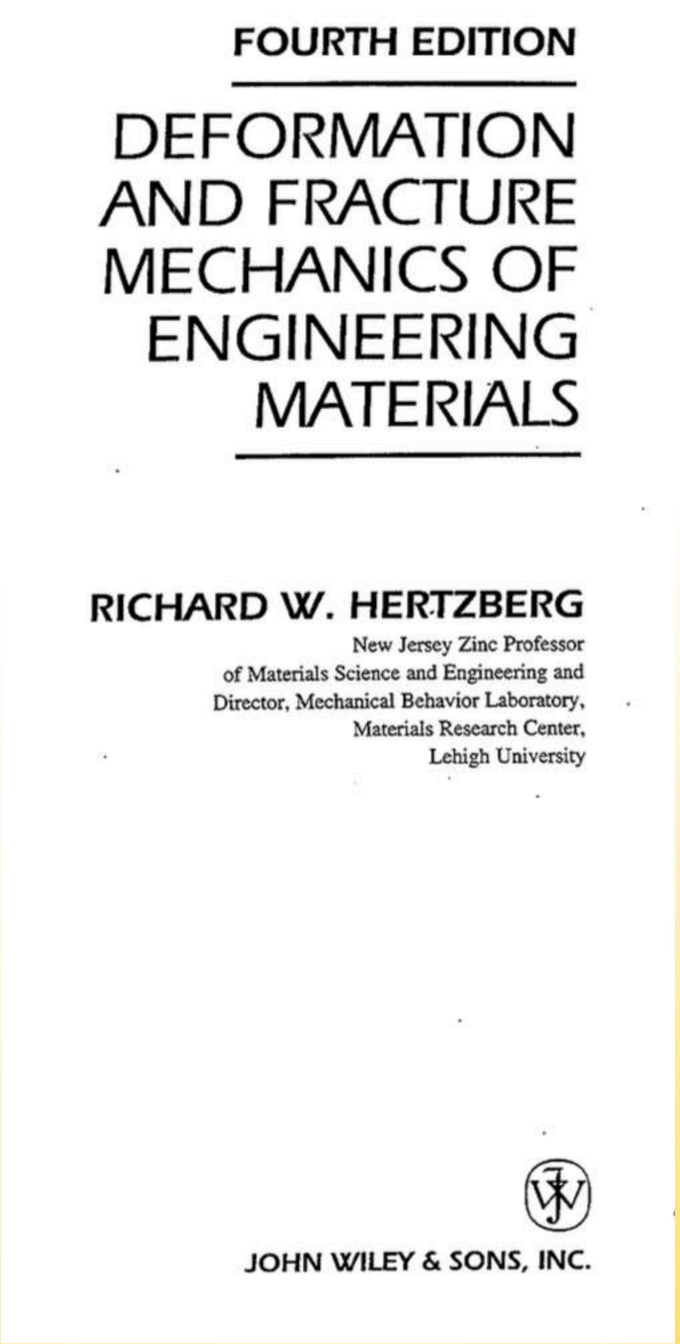

FOURTH EDITION

DEFORMATION
AND FRACTURE
MECHANICS OF
ENGINEERING
MATERIALS

RICHARD W. HERTZBERG
New Jersey Zinc Professor
of Materials Science and Engineering and
Director, Mechanical Behavior Laboratory,
Materials Research Center,
Lehigh University

JOHN WILEY & SONS, INC.

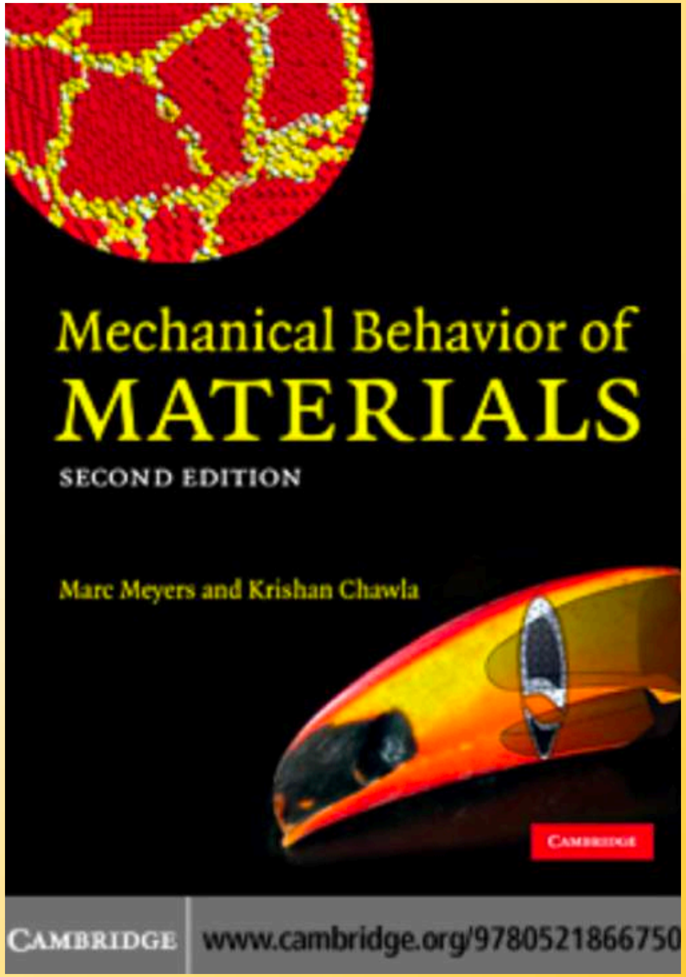

Mechanical Behavior of
MATERIALS
SECOND EDITION

Marc Meyers and Krishan Chawla

CAMBRIDGE

CAMBRIDGE www.cambridge.org/9780521866750